

Network-Optimised Spiking Neural Network for Event-Driven Networking

Muhammad Bilal

School of Computing and Communications, Lancaster University, LA1
4WA Lancaster, United Kingdom
m.bilal@ieee.org

Abstract

Time-critical networking requires low-latency decisions from sparse and bursty telemetry, where fixed-step neural inference waste computation. We introduce Network-Optimised Spiking (NOS) ¹, a two-state neuron whose variables correspond to normalised queue occupancy and a recovery resource. *NOS* combines a saturating excitability nonlinearity for finite buffers, service and damping leaks, graph-local inputs with per-link gates and delays, and differentiable resets compatible with surrogate gradients and neuromorphic deployment. We establish existence and uniqueness of subthreshold equilibria, derive Jacobian-based local stability tests, and obtain a scalar network stability threshold that separates topology from node physics through a Perron-mode spectral condition. A stochastic arrival model aligned with telemetry smoothing links *NOS* responses to classical queueing behaviour while explaining increased variability near stability margins. Across chain, star, and scale-free graphs, *NOS* improves early-warning F1 and detection latency over MLP, RNN, GRU, and temporal-GNN baselines under a common residual-based protocol, while providing practical calibration and stability rules suited to resource-constrained networking deployments.

keywords

Spiking neural networks, Congestion control, Active queue management, Explicit Congestion Notification, Network stability, Spectral graph theory, Distributed control, Queueing theory

1 Introduction

Machine learning has reshaped core networking tasks, including short-horizon traffic forecasting, anomaly detection, and routing optimisation. Conventional deep models such as multilayer perceptrons, recurrent networks, and graph neural networks perform well when labels are plentiful and training is done offline. Spiking neural networks (SNNs)

¹<https://mbilal84.github.io/nos-snn-networking/>

offer a complementary path. Their event-driven computation is naturally sparse in time and energy, which aligns with packet-level operation at the edge and in devices with tight power budgets. Recent surveys and hardware results report large efficiency gains for spiking workloads on neuromorphic substrates, motivating designs that couple spiking dynamics to network semantics [6, 7, 5]. Foundational work on temporal coding and computational power further motivates spike-based processing in control settings [20]. In parallel, hardware platforms such as Intel’s Loihi and its toolchain demonstrate on-chip learning and practical workflows for deploying SNNs [7, 22].

Classical SNNs, while powerful for neuroscientific exploration, are poorly matched to networking practice due to several fundamental limitations. Firstly, they often prioritize biological analogy, defining abstract internal states rather than variables with direct network interpretations like queue occupancy, service rate, or link delay [14] [27]. This biological focused modeling also leads to dynamics that present optimization challenges; the hard threshold-and-reset dynamics intrinsic to spiking neurons create a non-differentiable discontinuity that obstructs gradient-based optimisation, a cornerstone of modern machine learning [1][38]. Furthermore, the treatment of topology and per-link quality is often implicit or uniform, neglecting the complex, heterogeneous, and weighted graphs that define real-world networks. From a dynamical systems perspective, the excitability in common SNN models formulation can be unbounded, leading to unrealistic behaviour under high input load and presenting significant numerical instability [37]. Finally, implementations face practical limits in training cost, input encoding, and deployment on resource-constrained neuromorphic or edge hardware. Consequently, evaluation remains limited, often failing to bridge the gap between abstract simulations and performance on real network topologies and traffic patterns [14] [36]. Classical spiking and queueing-inspired models, including Hodgkin–Huxley [15], Izhikevich [17] and G-networks [10], either impose heavy dynamics or lack graph-aware, differentiable, queue-semantics. These gaps motivate a compact spiking unit whose state maps to normalised queue occupancy and recovery, whose inputs are graph-local with delays and optional per-link gates, and whose reset is differentiable for gradient-based optimisation [38]. A second driver is deployment. Neuromorphic systems such as Intel’s Loihi families demonstrate on-chip learning rules, synaptic delays, and event-driven execution that can reduce energy for small edge workloads while keeping latency low [7]. Related SNN studies in robotics and generic complex-network settings illustrate broader interest in topology and control, but their objectives differ from packet dynamics and queue semantics considered here [39, 32, 21]. Such systems reinforce the case for spiking designs that expose measurable parameters and training handles, so that network operators can calibrate models from telemetry and run them under tight power envelopes. An extended comparison of when spiking neural networks are preferable to conventional ML and GNN models for networking tasks is given in *methods* A, while B reviews three classical spiking paradigms and evaluates their suitability for queue semantics, topology and trainability in packet networks.

Contributions and Findings. This article develops a *Network-Optimised Spiking* neuron (NOS) and examines its behaviour from single node to network scale. The model is compact and two-state, with each state and parameter tied to measurable network quantities. Queue occupancy serves as the fast state, and a slower recovery variable captures post-burst slowdown. Service appears as leak terms. Inputs are graph-local with options for per-link gating and fixed delay. A saturating nonlinearity prevents

unbounded growth and represents finite buffers. Two differentiable reset strategies are introduced—an event-triggered exponential soft reset and a continuous pullback shaped by a sigmoid—both enabling gradient-based training while preserving spiking dynamics.

The analysis gives equilibrium existence and uniqueness, stability tests from the Jacobian, and a network threshold that scales with the Perron eigenvalue of the coupling matrix. Saturation enlarges the stable region by reducing the effective excitability slope. An operational margin links damping with offered load and provides a two-parameter contour for planning and capacity checks. Stochastic arrivals are represented as shot noise or compound Poisson input with calibrated scales. Practical guidance covers parameter initialisation from telemetry, surrogate-gradient training with a homotopy in reset sharpness, and deployment on neuromorphic platforms, are detailed in *methods* C, D and D.1, respectively. The evaluation protocol uses label-free forecasting with residual-based event scoring, in line with established practice in time-series anomaly detection.

Findings show that bounded excitability yields unique single-node equilibria and wider stability regions than the unbounded quadratic drive. Network stability follows the Perron eigenvalue, giving a direct means of control through weight normalisation and topology choice. Differentiable resets remove optimisation difficulties caused by hard jumps and enable surrogate-gradient training without disturbing event timing. In residual-based forecasting, *NOS* acts as a physics-aware forecaster, achieving competitive accuracy and latency on chain, star, and scale-free graphs while remaining interpretable and suitable for neuromorphic execution.

Results

2 Proposed model: Network-Optimised Spiking neural network (*NOS*)

Networking workloads are shaped by graph structure, finite buffers, and service constraints, and they must be trainable from telemetry. We therefore begin with graph-local inputs that respect neighbourhoods and link heterogeneity,

$$I_i(t) = \sum_{j \in \mathcal{N}(i)} w_{ij} S_j(t), \quad (1)$$

where $S_j(t)$ is a presynaptic event train and w_{ij} encodes link capacity, policy weight, or reliability. Three implementation choices motivate the *NOS* design. First, the reset must be continuous and differentiable so gradient-based training is possible. Second, state variables and parameters should map to observables such as normalised queue length, service rate, and recovery time. Third, subthreshold integration needs explicit stochastic drive so gradual load accumulation and burstiness are both represented. Implementation-level choices, detailed calibration rules, and additional parameter-tuning heuristics, including the pipeline in Fig. 6, are summarised in *methods* D.

2.1 Variable reinterpretation

We define a two-variable *NOS* unit whose excitability and recovery states encode the short-term behaviour of a networked queue. The fast state $v_i(t)$ represents a normalised

queue or congestion level, with $v_i \in [0, 1]$ mapping empty to full buffer. The slow state $u_i(t)$ represents a recovery or slowdown resource that builds during bursts and relaxes thereafter.

$v \mapsto$ normalised queue length or congestion level, $u \mapsto$ recovery or slowdown resource.

Here $v = 1$ corresponds to a full buffer. The state u summarises pacing, token replenishment, or rate-limiter cool-down that follows a burst. This choice allows direct initialisation from traces: v from queue occupancy, u from measured relaxation time, and the link between them from decay after micro-bursts. It also clarifies units. Both v and u evolve in the same time scale, which keeps linearisation and stability analysis transparent.

2.2 State variables and dynamics

For each node i we adopt a bounded excitability function and explicit damping:

$$\frac{dv_i}{dt} = f_{\text{sat}}(v_i) + \beta v_i + \gamma - u_i + I_i(t) - \lambda v_i - \chi(v_i - v_{\text{rest}}), \quad (2)$$

$$\frac{du_i}{dt} = a(bv_i - u_i) - \mu u_i = abv_i - (a + \mu)u_i. \quad (3)$$

with bounded excitability

$$f_{\text{sat}}(v) = \frac{\alpha v^2}{1 + \kappa v^2}, \quad (4)$$

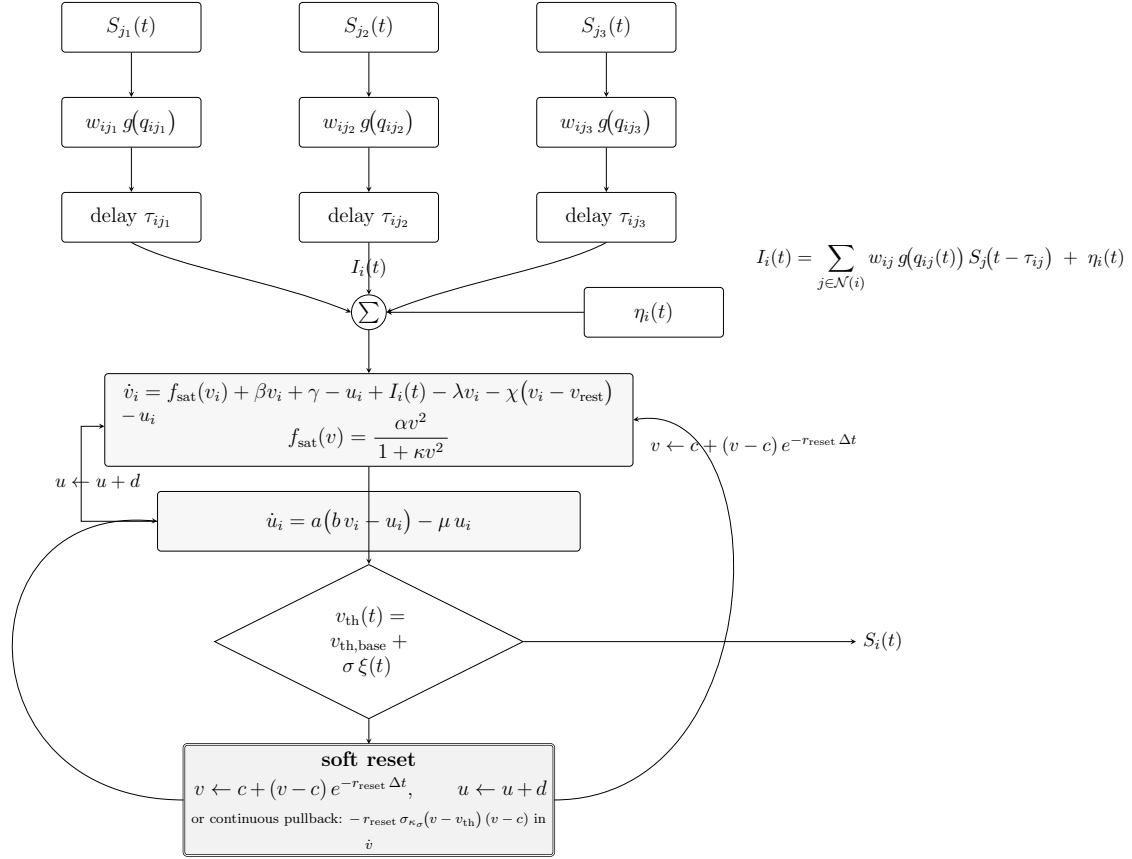
Equation (2) separates four operational effects. The term $f_{\text{sat}}(v_i)$ (see (5)) captures the convex rise of backlog during rapid arrivals while remaining bounded. The linear part $\beta v_i + \gamma$ fits residual slope and offset that are visible in practice after removing coarse trends. The coupling $-u_i$ models recovery drag that slows re-accumulation immediately after events. Finally, $-\lambda v_i - \chi(v_i - v_{\text{rest}})$ represents service and small-signal damping. Equation (3) integrates recent congestion with sensitivity ab and relaxes at rate $a + \mu$. Thus, the *NOS* model reflects three intuitive aspects of queue behaviour: the rise under increasing load, the draining through service, and the short-lived slowdown that follows bursts. Fig. 1 illustrates a single *NOS* unit, highlighting its graph-local inputs, excitability dynamics, recovery variable, stochastic threshold, and differentiable reset pathway. Spike generation and reset principles are discussed in *methods* E. Operational interpretations and data-driven initialisation rules for all *NOS* parameters are summarised in Table 3 in *methods* C, with further design guidance in *methods* D.

2.3 Bounded excitability

We replace the unbounded quadratic drive in Izhikevich model by a saturating nonlinearity

$$f_{\text{sat}}(v) = \frac{\alpha v^2}{1 + \kappa v^2}, \quad \alpha > 0, \kappa > 0. \quad (5)$$

For small queues this behaves approximately quadratically, while for large queues it saturates at α/κ , which enforces a finite growth rate and reflects finite buffer capacity. Detailed small-signal approximations, derivative bounds, and their use in stability margins are given in *methods* F.



Per-link weight and gate $w_{ij} g(q_{ij})$, delay τ_{ij} , and shot-noise $\eta_i(t)$ feed a node with bounded excitability f_{sat} , recovery u_i , stochastic threshold, and differentiable reset. The threshold emits $S_i(t)$; reset updates feed back into v and u .

Figure 1: NOS unit with graph-local inputs, weighted per-link gates and delays, exogenous shot-noise, bounded excitability, recovery dynamics, stochastic threshold, and differentiable reset. Three non-overlapping lanes: left for $u \rightarrow v$, centre for $v \rightarrow v_{\text{th}}$, right for reset $\rightarrow v$.

2.4 Graph-local inputs, explicit delays, and per-link queues

Topology enters through delayed presynaptic events (neighbourhood wiring, per-link delays, and optional link-state gates that modulate influence during congestion, scheduling, or wireless fading). Starting from (1), we incorporate delays and exogenous noise as

$$I_i(t) = \sum_{j \in \mathcal{N}(i)} w_{ij} S_j(t - \tau_{ij}) + \eta_i(t), \quad (6)$$

where $\mathcal{N}(i)$ is the graph neighbourhood of node i , $S_j(t - \tau_{ij})$ is the presynaptic event train as it arrives at node i , w_{ij} encodes a link's nominal capacity, policy weight, or reliability, τ_{ij} is a link delay, and $\eta_i(t)$ is stochastic drive. The statistical properties of these stochastic drives, and their impact on variance and delay tails, are quantified through experiments in the *methods*, particularly *methodss* G.1 and H. In this work we treat $\eta_i(t)$ as a bursty arrival process and obtain τ_{ij} and w_{ij} from simple measurements such as round trip times and link utilisation statistics. The full statistical specification of the exogenous drive, the calibration of delays and weights, and the optional link state gates based on $q_{ij}(t)$ are given in *methods* I and J.

3 Equilibrium and local stability analysis

Using the properties of the bounded excitability function in *methods* F, the existence and uniqueness conditions for the subthreshold equilibrium and the detailed stability proofs are developed in *methods* K. At equilibrium a *NOS* node holds a steady queue level set by arrivals, service, and graph-local coupling. Solving the stationarity conditions $\dot{v}_i = \dot{u}_i = 0$ yields a scalar fixed-point equation balancing bounded excitability, linear drain, and a constant baseline from $\gamma + \chi v_{\text{rest}} + I_i^*$. Under the same service-dominance requirement as in Corollary 2.1, this equation admits a unique operating point $v_i^* \in [0, 1]$ for each admissible mean drive I_i^* ; the full derivation and small-signal approximations are given in *methods* K.1.

3.1 Equilibrium equations

For node i the subthreshold equilibrium (v_i^*, u_i^*) is obtained by solving $\dot{v}_i = \dot{u}_i = 0$. Eliminating u_i^* gives a scalar balance between bounded excitability, linear drain and a baseline term that absorbs γ , v_{rest} and the mean drive I_i^* . Under a mild service dominance condition the resulting fixed point is unique in $[0, 1]$ for each admissible I_i^* (*methods* K.1).

3.2 Jacobian and linear stability

Linearising a *NOS* node about a subthreshold equilibrium (v^*, u^*) produces a 2×2 Jacobian whose entries depend on the small signal slope $f'(v^*)$ and the coefficients $(\lambda, \chi, a, b, \mu, \beta)$. Standard trace and determinant inequalities then yield local stability conditions that tie the damping provided by λ and χ to the maximum admissible slope of f_{sat} (*methods* K.2).

3.3 Network coupling and global stability

In isolation a *NOS* unit settles to a load-service balance set by its local parameters. In a network the steady input I_i^* is shaped by neighbours and policy weights, so existence and robustness of equilibria depend on both the operating point and the coupling matrix W . Bounds on I_i^* in terms of matrix norms of W lead to sufficient existence conditions that expose how heavy fan-in or large policy weights shrink headroom for a given steady drive.

A convenient scalar “operational margin” summarises these existence bounds in terms of subthreshold damping χ and the maximum steady input $I_{\text{max}} = \max_i I_i^*$. Positive margin corresponds to safe operation with headroom for burstiness; margin near zero signals proximity to loss of equilibrium. The trade-off between damping and sustained load is illustrated in Fig. 2, while the full inequalities and derivations are given in *methods* K.3, and the associated bifurcation structure and parameter trends (saddle-node versus Hopf onsets) are summarised in *methods* L.

3.4 Block Jacobian, network spectrum, and stability threshold

Linearising the coupled *NOS* network about a subthreshold equilibrium yields a $2N \times 2N$ block Jacobian whose dominant network contribution is proportional to $g \rho(W) f'_{\text{sat}}(v^*)$, where g is a global coupling gain and $\rho(W)$ is the spectral radius of the coupling matrix.

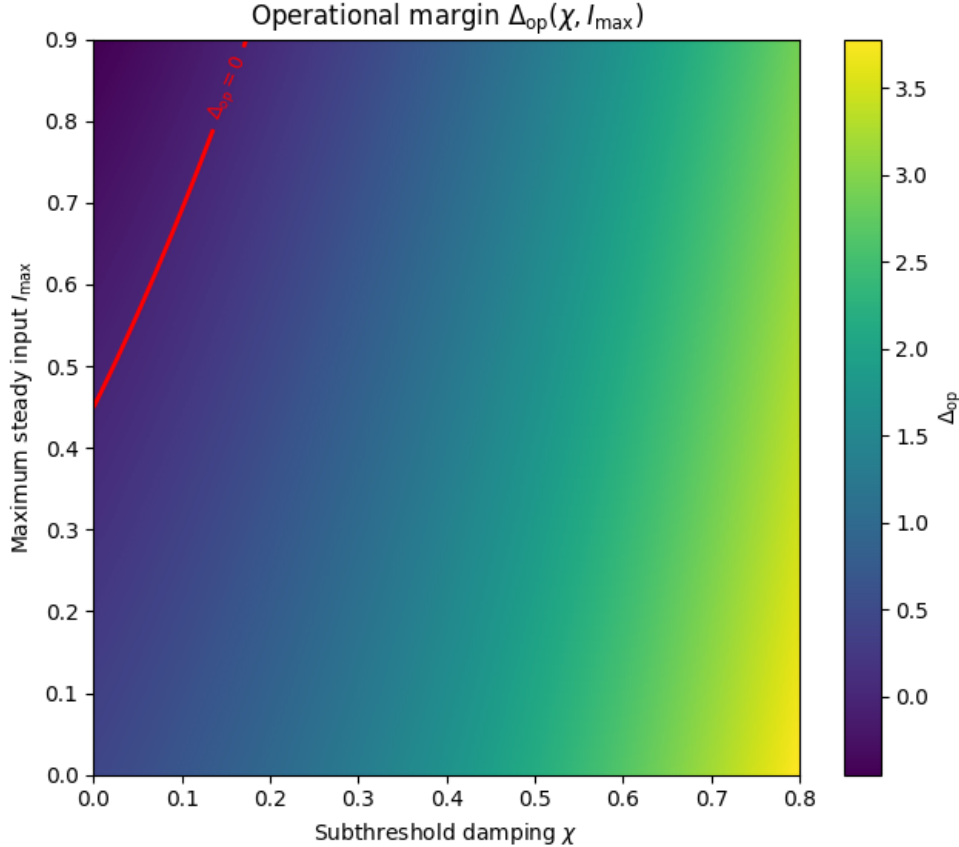


Figure 2: Operational margin $\Delta_{\text{op}}(\chi, I_{\text{max}})$ as a function of subthreshold damping χ and maximum steady input $I_{\text{max}} = \max_i I_i^*$. The red contour marks $\Delta_{\text{op}} = 0$; points above this curve (larger I_{max} for the same χ) lie beyond the small-signal existence bound. Parameters $\{\alpha, \kappa, \lambda, \beta, a, b, \mu, \gamma, v_{\text{rest}}\}$ are held fixed as in the text. *methods* K.3 gives the analytical definition of Δ_{op} and one-dimensional sweeps versus I_{max} , together with sensitivity to $\rho(W)$ and g .

The analysis shows that the first loss of small-signal stability is well predicted by the scalar condition

$$g \rho(W) f'_{\text{sat}}(v^*) < \Lambda, \quad (7)$$

with Λ the net drain defined from the local coefficients (cf. (90)). Parameters are non-dimensionalised so that the stability proxy $g \rho(W) f'_{\text{sat}}(v^*) < \Lambda$ and the operational margin Δ_{net} are comparable across sites, as detailed in the *methods* N. This separates node physics from topology and matches the operational proxy used in Section 4. The full block Jacobian, Perron-mode reduction, numerical spectral validation, and Gershgorin-style bounds are given in *methods* K.4 and K.5, while *methods* L characterises the saddle-node and Hopf-onsets and shows that the instability threshold obeys the spectral collapse relation in (85).

4 Network-level stability and topology dependence

We simulate *NOS* networks with an event driven integrator that updates delayed spikes, state variables and thresholds for every node at each step. Pseudocode and implementa-

tion details, including optional stochastic arrivals and avalanche counting, are provided in the *methods* R.

4.1 Topologies and experiments

We tested *NOS* on large networks of size $N = 250$ with different canonical topologies:

Chain topology. Nodes are arranged in a linear sequence, representing serial bottlenecks such as routers on a backbone link. Propagation is slowed by distance, requiring stronger coupling for instability.

Star topology. One hub connects to all leaves, representing a single aggregation point such as a central switch. This configuration is fragile, as overload of the hub destabilises the entire structure.

Scale-free topology. Networks generated by the Barabási–Albert model capture heterogeneous connectivity with hubs and peripheries. This structure shows intermediate behaviour: hubs can initiate cascades, but leaves constrain their spread.

Figure 3 summarises the network-level phenomena captured by *NOS*. Panel (a) shows that when link delays are included ($\tau_{ij} > 0$), the stability boundary shifts: oscillations emerge at lower coupling k , reflecting how communication latency destabilises otherwise stable traffic. Panel (b) compares absolute resilience across topologies: chains require stronger coupling to destabilise, stars are fragile because of their single hub, and scale-free networks lie in between. Panel (b'') reframes this relative to the Perron spectral prediction. Here chains deviate strongly, sitting well above the $1/\rho(W)$ baseline, while stars and scale-free graphs align more closely. This means that spectral tools capture hub-dominated topologies reliably but underestimate the resilience of homogeneous chains. Additional synchrony measures based on a Kuramoto type order parameter and finite size trends are reported in *methods* O, shows $\langle R \rangle$ versus $k = g\rho(W)$ (Fig. 15) and the finite-size sharpening of the transition around the Perron prediction k^* . Together these results demonstrate that *NOS* bridges dynamical-systems formalism and networking dynamics. It shows where simple spectral theory suffices (hub-dominated topologies) and where explicit simulation is required (homogeneous or delayed structures).

4.2 Predictive baseline: comparison with machine learning models

Many operational networks lack reliable labels, so short-horizon forecasting with residual-based event inference is the standard route. We follow that practice. A complementary zero-shot comparison, in which all methods operate without supervised training and use only arrival-based calibration, is reported in *methods* P. We compare *NOS* with tGNN, GRU, RNN, and MLP under three canonical graphs: scale-free, star, and chain. Full details of the evaluation protocol are given in *methods* Q.

Figure 4 presents the test-range series with start markers for each method. A marker at the truth dot indicates a correct start, a marker to the right indicates a late start, and a marker to the left indicates an early start. Extra markers away from a truth dot are false positives, while missing markers in the vicinity of a truth dot are false negatives. Read across the three panels from scale-free to star to chain and the pattern is consistent. On

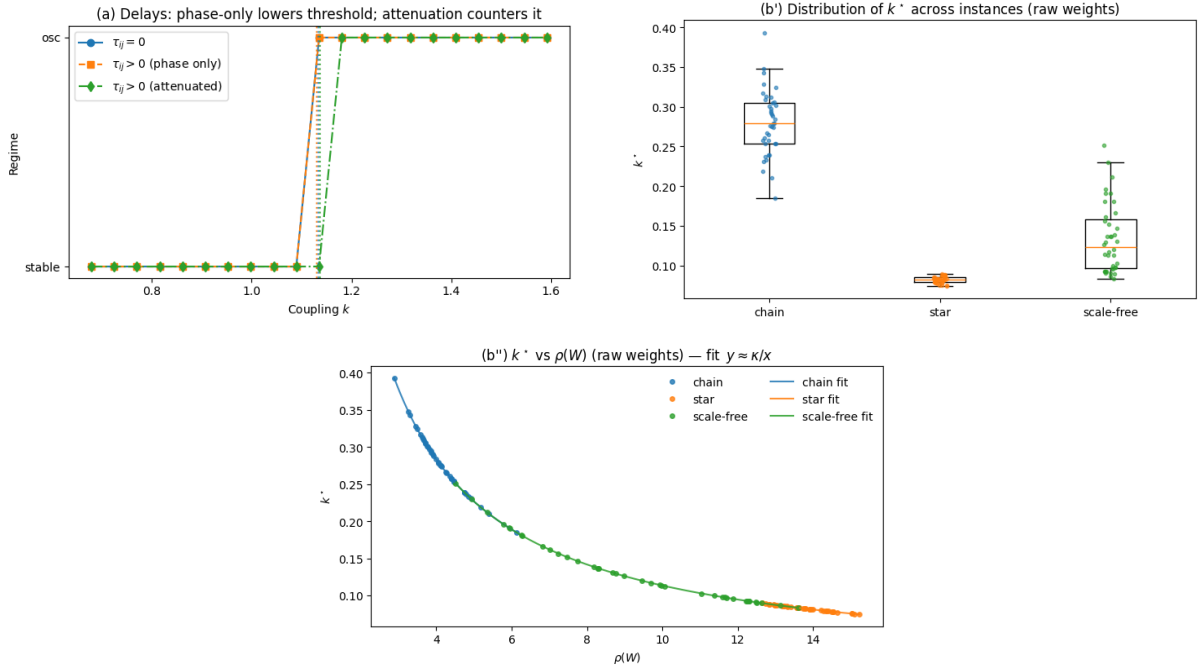


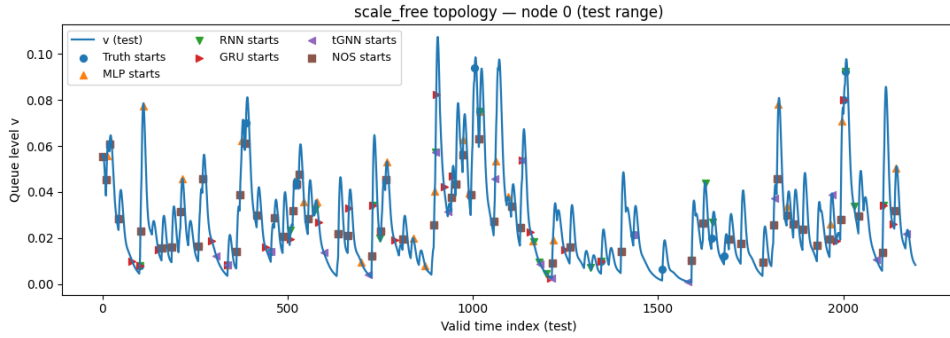
Figure 3: Network-level dynamics in *NOS*. **(a)** Delay effects: introducing link delays $\tau_{ij} > 0$ shifts the stability boundary, causing oscillations to emerge at lower coupling k . **(b)** Absolute topology effects: chain networks destabilise last (resilient), stars first (fragile), with scale-free in between. **(b'')** Relative to Perron-mode prediction: chain networks deviate strongly above the $1/\rho(W)$ line, while star and scale-free graphs track the prediction closely.

the scale-free graph, bursts arrive in clusters and ramps are steep. *NOS* remains close to the truth throughout these clusters and avoids small oscillations. The tGNN calls tend to appear inside the ramps, which shows up as slight right shifts. RNN produces occasional early calls on moderate slopes, and GRU sits between RNN and tGNN. MLP is the least selective and places extra markers on low-amplitude wiggles. Moving to the star graph, the hub concentrates load while spokes are quieter. This helps tGNN, yet *NOS* remains more selective at the spokes and keeps the timing tight when the hub rises. On the chain graph, onsets are clearer and repeat through the range. *NOS* lands on the main rises with few stray calls in the troughs, while tGNN shows a mild lag, RNN is a little early on shallow slopes, and GRU again lies between them. The visual story across the three topologies is that *NOS* aligns closely without over-firing when the background is quiet.

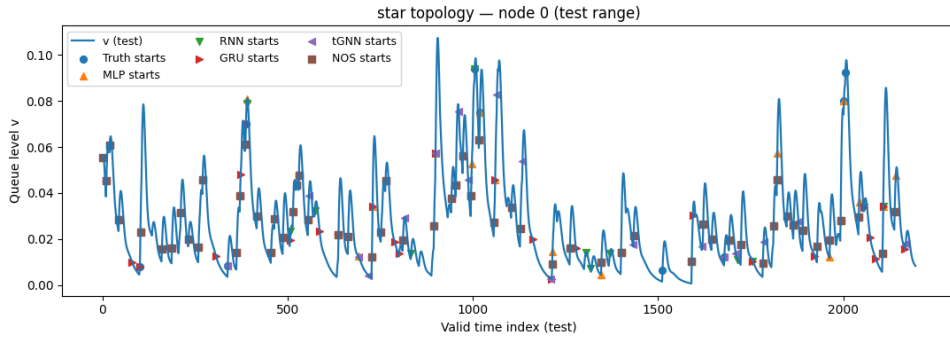
Figure 5 gathers the aggregate scores. The bars report F1, precision, and recall under the same train-calibrated residual protocol. The curves report one-step error as MAE and RMSE and the median start-latency in milliseconds. Higher bars indicate better detection quality. Lower curves indicate better forecasting accuracy and earlier response. Across all three topologies *NOS* attains the highest F1 by holding strong precision while lifting recall. It also yields the lowest MAE and RMSE and the smallest latency. RNN keeps good precision but loses recall and responds later. GRU and tGNN are intermediate and more sensitive to the graph structure. MLP has higher errors and longer delays. The metric panels match what the range plots suggested: *NOS* is both earlier and more selective, and its forecasts give cleaner residuals for thresholding.

These differences have direct operational meaning. High precision with weak recall

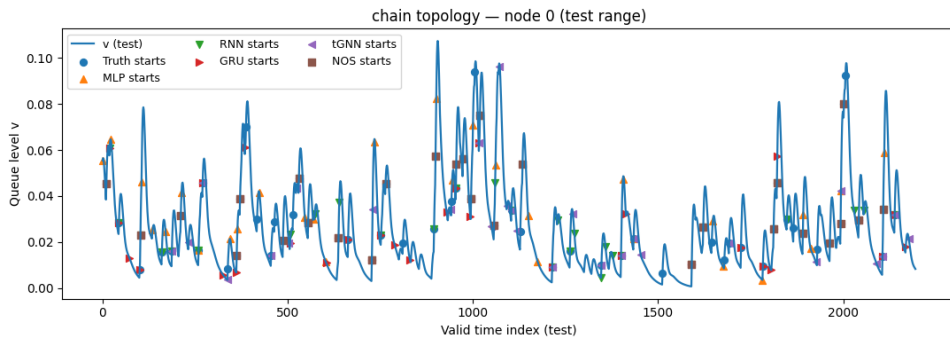
misses incidents that matter. High recall with weak precision floods operators with alarms. Lower forecast error stabilises residual scales and avoids threshold drift. Lower latency preserves time for pacing, admission, and rerouting. Taken together, the figures show that *NOS* gives an effective operating point across scale-free, star, and chain graphs. It preserves recall without inflating false positives and it warns early enough to act when load begins to rise.



(a) Scale-free. Truth and model start markers on the test range.

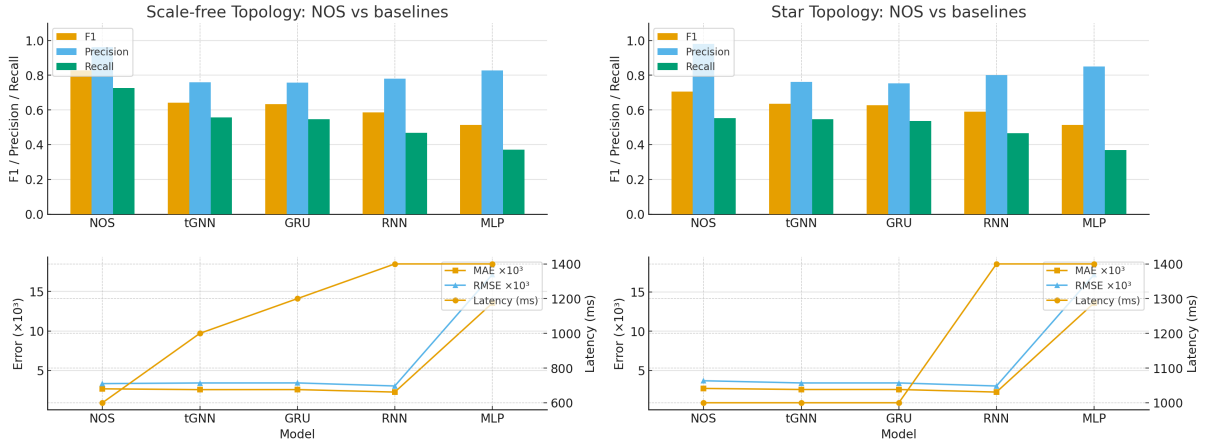


(b) Star. Truth and model start markers on the test range.

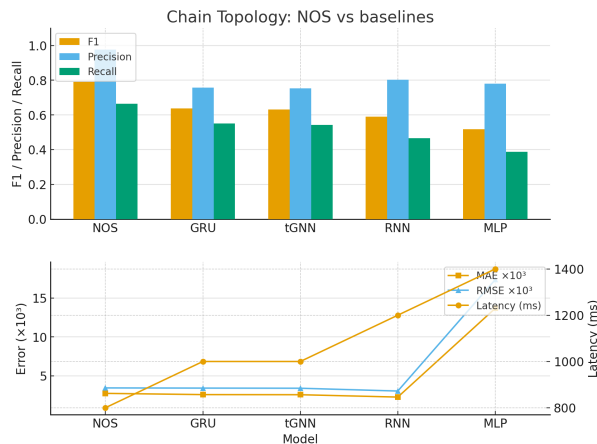


(c) Chain. Truth and model start markers on the test range.

Figure 4: Test-range alignments under train-calibrated residual thresholds. A marker at the truth dot is correct, to the right is late, to the left is early. Extra markers indicate false positives, and missing markers near truth indicate false negatives. *NOS* remains close to truth across all three topologies while avoiding small oscillations.



(a) Scale-free. F1, precision, recall, MAE, (b) Star. F1, precision, recall, MAE, RMSE, and median start-latency.



(c) Chain. F1, precision, recall, MAE, RMSE, and median start-latency.

Figure 5: Summary metrics under the label-free residual protocol. Higher bars are better for F1, precision, and recall. Lower curves are better for MAE, RMSE, and latency. *NOS* achieves the best F1, the lowest forecast error, and the earliest starts across all three topologies.

Discussion

NOS treats congestion monitoring and control as a compact spiking process whose ingredients are aligned with how networks are actually run. The queue proxy v is normalised to buffer fullness, the recovery state u encodes recent stress, excitability is bounded to keep queues within a finite envelope, and the linear drains λ and χ sit on the same device clocks as schedulers and EWMA filters. Thresholds implement budgeted alarms and resets are smooth enough for gradient-based training while still producing crisp, scheduler-scale events. Inputs are graph-local and carry explicit delays and per-link gates, so timing and residual capacity appear as first-class quantities rather than side effects of architecture.

The comparison with classical spiking paradigms clarifies what is gained. Random Neural Networks exploit product forms and queueing intuition but hinge on Poisson assumptions and stationary averages. Hodgkin–Huxley and Izhikevich offer rich excitable dynamics, yet their variables and parameters are tied to ion channels and generic cortical

behaviour rather than to queue occupancy, service, and link delay. Across these models, either the physics is faithful and heavy or it is light and disconnected from networking semantics. *NOS* occupies a middle ground. It keeps a two-dimensional state with a saturating excitability f_{sat} and a recovery loop, and it assigns queue-level meaning to every parameter that appears in the small-signal slope, stability tests, and reset dynamics. This mapping is the basis for the operational rules in the Online Methods.

The analytical results show that stability can be expressed in terms that are familiar to operators. At node level, the Routh–Hurwitz conditions reduce to a balance between the steepest local slope of $f_{\text{sat}}(v)$ and the effective drain $\Lambda = \lambda + \chi + ab/(a + \mu) - \beta$. At network level, coupling enters only through $g\rho(W)$, so the proxy $g\rho(W)f'_{\text{sat}}(v^*) < \Lambda$ cleanly separates topology from node physics. In practice this means that one can reason about headroom using three kinds of lever: adjust the graph through $\rho(W)$ by reweighting or sparsifying heavy fan-in, adjust the gain g on stressed regions through scheduling and policy, or adjust the local margin Λ through service, damping, and recovery parameters. The bifurcation and synchrony analyses confirm that this scalar picture captures the onset of both saddle–node tipping and Hopf-like oscillations, and the finite-size experiments show that the resulting thresholds sharpen with network size.

The queueing baselines anchor *NOS* against classical theory and device-level intuition. In open loop, light-load calibration aligns the *NOS* mean with the M/M/1 prediction, while the bounded excitability and soft pull-back cause earlier bending near saturation and much shorter tails under bursty MMPP arrivals. From a networking point of view, *NOS* trades a small increase in approximation error at high load for a systematic reduction in deep-queue probability, which is precisely where SLO violations and drop storms arise. In closed loop, *NOS*-based controllers produce marking signals that are decisive and low in jitter, avoiding both the noisy oscillations of raw queue marking and the lag introduced by heavy low-pass filtering. These behaviours are consistent with the analytical headroom conditions and with the linear decay times extracted from the local Jacobian.

The forecasting experiments indicate that *NOS* is competitive with compact learned baselines when labels are scarce. A fluid predictor driven by the same arrivals gives a strong MAE reference, since it essentially reproduces the queueing simulator. *NOS* does not attempt to mimic every backlog micro-fluctuation and therefore carries a larger point error, yet it delivers high event skill for burst onset detection and produces compact responses around excursions. Temporal GNNs, MLPs and GRUs trained in the same label-free regime tend to trade off noise suppression against timing accuracy. In contrast, the bounded, reset-driven dynamics of *NOS* grant sharp onset timing without extended false positives between bursts. The protocol is deliberately strict, with train-only calibration and validation-based thresholds, so these gains are unlikely to be artefacts of tuning.

The noise sensitivity and avalanche analyses view *NOS* through the lens of stochastic drive. Shot-noise arrivals with realistic smoothing produce firing statistics whose dependence on amplitude, coupling and recovery matches the linear response theory. As the network approaches the coupling threshold, the same noise leads to higher firing rate, larger inter-spike-interval variability and heavier avalanche tails. The fitted power-law exponents and the synchrony order parameter show that coupling can push the system toward scale-free congestion cascades along dominant influence paths. From an operational perspective, this confirms that the same levers that increase deterministic headroom also reduce susceptibility to noise-driven cascades: higher service and damping, earlier saturation through larger κ , and reduced effective coupling on noisy links.

A further aspect of the design is the explicit path to neuromorphic deployment. Address–event routing realises sparse, delayed coupling with the same W and τ_{ij} that appear in the analysis. Soft resets are implemented as leaky pull-backs without algebraic jumps, and fixed-point quantisation respects the queue normalisation used in software. The stability proxy carries over once finite precision errors are bounded, so the same margin checks can be applied when deploying on mixed-signal or digital neuromorphic substrates. This alignment between model, analysis and hardware is attractive for edge and in-network deployments where energy per decision must scale with activity rather than with link count.

Several limitations follow from our modeling choices. The arrival model uses compound Poisson shot noise with exponential smoothing, which captures burstiness at the timescales of typical telemetry but does not represent long-range dependence or heavy-tailed flow mixing in full generality. The experiments focus on single-queue observables and fixed topologies, and the queueing baselines largely reflect M/M/1-style behaviour. Joint adaptation with transport protocols, multi-queue schedulers and cross-layer policies remains to be explored. Training uses surrogate gradients and truncated BPTT windows aligned with the recovery time. Although the homotopy schedule and clipping rules stabilise optimisation, a more systematic study of learnability under aggressive thresholds and high coupling would be valuable.

Future work can proceed along three directions. First, richer traffic and topology models, including multi-tenant datacentre fabrics and radio access networks with mobility, would test the robustness of the stability proxy and the forecasting claims. Second, coupling *NOS* units with GNN or RL controllers in a principled hierarchical design would realise the complementary roles discussed in the introduction, with *NOS* providing fast, local reflexes and deep models orchestrating global policy. Third, hardware-in-the-loop studies on contemporary neuromorphic platforms would allow a direct comparison of energy and tail performance against software-only baselines. Together, these steps would clarify whether *NOS* can serve as a practical building block for AI-native networks in production rather than only as an analytic and experimental tool.

Methods

A Spiking Neural Networks for Networking: Scope and Complementarity

Spiking models describe a time-varying state and emit discrete events when a threshold is crossed. In the biological literature this is written in terms of a membrane potential $V(t)$; for networking the same idea can be read as a state that advances under inputs and intrinsic dynamics until an event is produced. The event acts as the computational primitive. Intelligent networking has been led by deep learning, reinforcement learning, and graph neural networks trained on aggregates or labelled flows. These methods assume synchronous batches and centralised compute. Spiking neural networks use event-driven updates, which aligns with irregular packet arrivals, bursty congestion, and anomaly signatures that depart from baseline rather than average behaviour. The practical question is when this alignment matters enough to prefer an SNN, and when conventional ML or GNNs remain the better tool, 1 summarizes it.

Table 1: Comparative suitability of SNNs and conventional ML/GNNs across networking problem domains.

Problem domain	More suitable with SNNs	More suitable with ML/GNNs
Anomaly detection (e.g., DDoS, worm outbreaks)	Event-driven detection of sudden bursts; low-latency alarms [25, 4]	Flow-level detection from large corpora; supervised and deep models [2, 18]
Routing optimisation	Local adaptation in ad hoc or sensor settings using local rules; energy- and event-efficient deployment on neuromorphic hardware [7, 8]	Global path optimisation and traffic engineering with topology-wide objectives; GNN/RL controllers [35]
QoS prediction (throughput, delay)	Edge-side reaction to micro-bursts under power limits (event-driven inference) [7]	Predictive modelling from aggregates; offline/online regression and forecasting [13, 3, 34]
Traffic classification	Temporal signatures (periodicity, jitter) via spike timing and event patterns [30, 29]	Feature-rich flow classification with labels using CNN/RNN/GNN [28, 40, 33]
Wireless resource allocation	Local duty-cycling, sensing, and lightweight on-device decision-making under tight energy budgets [8]	Centralised spectrum allocation and large-scale optimisation with RL/GNN [24, 41, 16]
Network resilience and fault detection	Distributed detection of local failures and sudden state changes in streams [25, 4]	Correlating failures across topology; resilience modelling and recovery for SDN/CPS [26, 31, 23]

Event-driven versus batch-oriented learning. Packet systems are inherently event-driven. Conventional pipelines buffer into fixed windows before inference, adding latency and energy. SNNs update on arrival, so a single event can trigger a decision without waiting for a batch. This is attractive for anomaly alerts and micro-burst monitoring where early reaction is valuable.

Energy and deployment constraints. Edge devices and in-network elements often face tight power and memory budgets. Neuromorphic platforms (e.g., Loihi and SpiN-Naker) report energy advantages for spiking workloads, which supports in situ decisions at low latency [7, 9]. In contrast, data-centre controllers and core routers, with ample power and global context, typically profit from conventional ML and GNNs.

Temporal coding and traffic structure. Some networking tasks hinge on timing patterns rather than sheer volume: jitter in interactive media, periodic bursts in games, or hotspot prediction from inter-arrival times. SNNs encode such structure in spike timing and phase. Recurrent deep models can capture time as well, but temporal coding is native to spiking dynamics.

Local learning and autonomy. Networks are distributed. Routers, base stations, and sensors often adapt with limited scope. SNNs admit local rules such as spike-timing-dependent plasticity (STDP), enabling on-node adaptation. Global optimisation over topology and multi-objective trade-offs remains a strength of GNNs and reinforcement learning.

Complementary roles. SNNs and conventional AI are complementary. SNNs provide efficient, event-driven reflexes for local, time-critical decisions under tight budgets. Deep learning and GNNs act as global planners that integrate structure and statistics. A practical design places SNNs in edge nodes or programmable switches for reflexive response, coordinated with ML/GNN controllers for end-to-end policy.

B Classical spiking paradigms and networking suitability

This section reviews three classical spiking neural networks and examines what they offer, and their suitability for networking tasks where queue semantics, topology, and trainability plays important role.

B.1 Random Neural Network (Gelenbe)

The Random Neural Network (RNN) treats each neuron as an integer-valued counter driven by excitatory and inhibitory Poisson streams and yields a product-form steady state [11]. Let $q_i = \Pr\{k_i > 0\}$ denote the activity of neuron i . In steady state

$$q_i = \frac{\Lambda_i^+}{r_i + \Lambda_i^-}, \quad (8)$$

$$\Lambda_i^+ = \lambda_i^+ + \sum_j q_j r_j p_{ji}^+, \quad \Lambda_i^- = \lambda_i^- + \sum_j q_j r_j p_{ji}^-, \quad (9)$$

and the joint distribution factorises as $\Pr[k_1, \dots, k_N] = \prod_i (1 - q_i) q_i^{k_i}$.

The queueing affinity and fixed points make calibration attractive. However, backbone and datacentre traces are overdispersed and often long-memory, so a stationary product form understates burst clustering and tail risk. This follows from the Poisson and exponential assumptions of the model, which wash out temporal correlation and refractoriness. Product-form results emphasise stationarity, whereas operations rely on transient detection and control. Parameters r_i and p_{ji}^\pm do not tie directly to per-link capacity, delay, or gating. Under strong excitation, the signal-flow equations can fail to admit a valid solution with $q_i < 1$, leading to instability or saturation; when a solution exists it is unique [11, 12].

B.2 Hodgkin–Huxley

The Hodgkin–Huxley (HH) equations provide biophysical fidelity through voltage-gated conductances and reproduce spikes, refractoriness and ionic mechanisms [15]. The membrane and current relations are

$$C_m \frac{dV}{dt} = -(I_{\text{Na}} + I_{\text{K}} + I_L) + I_{\text{ext}}, \quad (10)$$

$$I_{\text{Na}} = \bar{g}_{\text{Na}} m^3 h (V - E_{\text{Na}}), \quad I_{\text{K}} = \bar{g}_{\text{K}} n^4 (V - E_{\text{K}}), \quad I_L = \bar{g}_L (V - E_L), \quad (11)$$

$$\frac{dx}{dt} = \alpha_x(V)(1 - x) - \beta_x(V)x, \quad x \in \{m, h, n\}. \quad (12)$$

where V is membrane potential; C_m membrane capacitance. $I_{\text{Na}}, I_{\text{K}}, I_L$ are sodium, potassium, and leak currents; I_{ext} is external or synaptic input. \bar{g}_{ion} are maximal conductances and E_{ion} reversal potentials. $m, h, n \in [0, 1]$ are gating variables with voltage-dependent rates $\alpha_x(V), \beta_x(V)$.

Hodgkin–Huxley offers mechanistic fidelity and a broad repertoire of excitable behaviour, and recent results show that HH neurons can be trained end to end with surrogate gradients, achieving competitive accuracy with very sparse spiking on standard neuromorphic benchmarks [19]. This confirms feasibility for learning and suggests potential efficiency from activity sparsity. For network packet-level control, the obstacles are practical rather than conceptual. The model comprises four coupled nonlinear differential equations with voltage-dependent rate laws, which typically require small timesteps and careful numerical treatment; in practice this raises computational cost and stiffness at scale, and training can fail without tailored integrators and schedules [19]. There is also no direct mapping from biophysical parameters to queue occupancy, service rate, or link delay, so calibration from network telemetry lacks interpretability. Taken together, HH remains a benchmark for cellular electrophysiology [15], but it is a poor fit for networking tasks that requires lightweight, semantically mapped states and trainable dynamics.

B.3 Izhikevich

The Izhikevich model balances speed and diversity of firing patterns [17]. Its dynamics and reset are

$$\frac{dv}{dt} = 0.04v^2 + 5v + 140 - u + I, \quad \frac{du}{dt} = a(bv - u), \quad (13)$$

$$\text{if } v \geq 30 \text{ mV} : \quad v \leftarrow c, \quad u \leftarrow u + d. \quad (14)$$

where, v is the membrane potential (mV). u is a recovery variable with the same units as v that aggregates K^+ activation and Na^+ inactivation effects. I is the input drive expressed as an equivalent voltage rate (mV ms^{-1}). The spike condition is $v \geq 30$ mV, after which $v \leftarrow c$ and $u \leftarrow u + d$. a is the inverse time constant of u (ms^{-1}); b is the coupling gain from v to u (dimensionless); c is the post-spike reset level of v (mV); d is the post-spike increment of u (mV).

The Izhikevich model achieves breadth of firing patterns with two state variables and a hard after-spike reset (13)–(14). This efficiency is documented through large-scale pulse-coupled simulations and parameter recipes for cortical cell classes. For networking, three constraints matter. First, the quadratic drift in (13) is not intrinsically saturating, which is mismatched to finite-buffer behaviour and can drive unrealistically rapid growth

between resets under heavy input. Second, the reset in (14) is discontinuous, which hinders gradient-based optimisation. Third, the parameters (a, b, c, d) are phenomenological and the connectivity is generic, so queue occupancy, service rate, link delay, and per-link quality are not first-class. These features explain the model’s value for neuronal dynamics and its limited interpretability for packet-level control.

B.4 Synthesis

Across the three formalisms the evidence points to the same gaps. Either the model is correct but heavy, or it is fast but carries non-differentiable resets and unbounded excitability. In all cases the parameters do not align with queue occupancy, service, and delay. Topology and per-link quality are usually implicit rather than explicit. For packet networks this limits interpretability, stability under high load, and the ability to train or adapt in situ. These observations set the design brief for NOS: a compact two-state unit with finite-buffer saturation, a service-rate leak and a differentiable reset, graph-local inputs with delays and optional gates, and parameters that map to observable network quantities.

Table 2: Classical paradigms versus networking requirements.

	RNN (Gelenbe)	Hodgkin–Huxley	Izhikevich
State/parameters map to queue, service, delay	Limited (probabilistic rates)	No	No
Trainability for control (gradients)	Moderate at steady state	Low	Low (non-differentiable reset)
Topology and per-link attributes explicit	Limited	No	No
Finite-buffer realism / stability under load	Stationary focus	Realistic but heavy	Unbounded drive
Edge-side compute/energy	Low–moderate	High	Low

C Admissible parameter region and calibration conventions

NOS parameters are summarised in Table 3, while Table 4 records the admissible region explored in our experiments. The entries are expressed on the experimental scale used throughout the paper, with queue fullness normalised to $v \in [0, 1]$ and a sampling bin of 5 ms. Rates given “per bin” convert to per second by multiplying by 200. We separate

structural constraints from initialisation choices so that the table serves reproducibility without implying narrow tuning.

The bounds have three roles. First, they enforce the normalisation and sampling assumptions used by the model and code. Second, they keep the sufficient stability condition from Lemma 2 satisfied with margin for the operating regimes we test. Third, they define a common hyperparameter space for stress tests across the three graph families. Within this region we draw values uniformly unless stated and refine only on the validation split.

Coupling and reset are disambiguated. The network coupling index is $k_{\text{net}} = g \rho(W)$, where $\rho(W)$ is the spectral radius after normalisation to $\rho(W) = 1$ and g is the scalar applied during experiments. The symbol k_{reset} denotes the sharpness of the soft reset gate and is independent of k_{net} . Delays τ_{ij} are given in milliseconds and reflect link propagation on the chosen binning. Shot-noise parameters (ν_i, A) match the noise sensitivity experiments and allow drive strength to approach the near-threshold regime without violating the stability bound.

The ranges for $\alpha, \kappa, \beta, \gamma$ control the shape and slope of the bounded excitability f_{sat} . The leak terms λ and χ set the small-signal decay about v_{rest} and are bounded to keep subthreshold dynamics stable at the 5 ms resolution. Recovery parameters (a, b, μ) govern post-burst relaxation and are given as per-bin rates. Threshold v_{th} , reset depth c , recovery jump d , and pullback speed ρ determine spiking and refractory behaviour. The mapping from arrivals to effective input uses an offset I_0 and a dimensionless gain, and may be optionally low-pass filtered with τ_s .

These bounds are admissible rather than prescriptive. Defaults used in the main text fall within Table 4 and are reported in the parameter-initialisation table. Sensitivity studies widening each bound by a factor of two preserve the relative ordering of methods on F1 and latency, with the largest trade-offs arising from λ and v_{th} as expected from precision–recall balance. All residual scalars and thresholds are fitted on train only, and validation is used to select per-node thresholds within the same admissible region.

D Design principles and engineering guidance

The *NOS* configuration is *straightforward*: it follows a small set of choices that mirror device behaviour in operational networks. Figure 6 summarises how a *NOS* unit is used in practice: telemetry pre-processing aligns with the smoothing in (40)–(43); the state (v, u) evolves by (2)–(3) with resets (27)/(28); events and residuals drive local detection and control; and spikes propagate over W with delays (6) to form neighbours’ inputs. This sets the stage for the engineering choices that follow (reset time scale, EWMA leak χ , gain scheduling g vs. $\rho(W)$, and threshold calibration).

For resets, one may use either an event-based exponential smoothing at threshold crossings or a continuous sigmoidal pullback that activates only above threshold (cf. §E); both are differentiable and avoid algebraic jumps, so gradient flow remains stable and attribution stays clear. In deployment terms, the return-to-baseline time is matched to the hardware drain or scheduler epoch, which means the model cools down on the same clock as the switch or NIC. Subthreshold prefiltering enters as a mild leak $\chi(v - v_{\text{rest}})$ that behaves like an EWMA on residual queues: it reveals early warnings while damping tiny oscillations caused by counter jitter, yet preserves micro-bursts that matter for control.

²Per-bin rates correspond to a 5 ms bin width. Multiply by 200 to convert to s^{-1} .

Table 3: Operational interpretation and *data-driven initialisation* of *NOS* parameters from observed network metrics. Defaults are starting values and a bin width of 5 ms; they are not hard limits.

Parameter	Observable(s)	Initialisation rule	Typical default
v	Queue length or buffer occupancy	Affine map full buffer $\rightarrow 1$, empty $\rightarrow 0$	—
v_{th}	False-alarm budget on residuals	Choose so $\Pr(z > z_\tau) = p_{\text{FP}}$ on train; set threshold at z_τ	0.60
λ	Mean service rate μ_{svc}	Per-bin rate: $\lambda \approx \mu_{\text{svc}} \Delta t$	0.18 per bin
χ	Small-signal damping	Fit AR(1) on subthreshold v : $v_{t+1} \approx (1 - \lambda - \chi)v_t + \dots$	0.02–0.05 per bin
β	Slope of dv/dt vs v	Regress $\Delta v/\Delta t$ on v on train residuals	0.05–0.8
γ	Baseline load	Intercept from the same regression, or set mean residual ≈ 0	0.06–0.10
α, κ	Nonlinear ramp steepness	Fit $f_{\text{sat}}(v) = \alpha v^2/(1 + \kappa v^2)$ to rising edges	$\alpha = 0.7, \kappa = 1.0$
a	Post-burst relaxation time τ_{rec}	$a \approx \Delta t/\tau_{\text{rec}}$ (per bin) from exponential fit	1.1 per bin
b	Recovery sensitivity to v	Tune so u tracks v during decay without overshoot	1.0–1.2
μ	Passive decay of u	Small regulariser on u drift; set by validation	0.05–0.15 per bin
c	Post-event baseline of v	Median v in a quiet window after events	0.10
d	Recovery jump on event	Choose to match observed refractory depth	0.20–0.30
k_{reset}	Desired sharpness of reset	Large enough to mimic hard reset without instability	14
r_{reset}	Reset time constant τ_{reset}	$r_{\text{reset}} \approx \Delta t/\tau_{\text{reset}}$ (per bin)	5 per bin
I_0, gain	Arrivals $\rightarrow I$ mapping	Regress I on smoothed arrivals: $I \approx I_0 + \text{gain} \cdot \text{arrivals}$	$I_0 = 0.10, \text{gain} = 1.0$
τ_s	Burst smoothing need	Low-pass if arrivals are spiky; choose cut-off by validation	0–10 ms
w_{ij}	Link rates/priorities	Proportional to nominal bandwidth or policy weight; normalise $\rho(W) = 1$	—
g	Desired coupling index k_{net}	Set $g = k_{\text{net}}/\rho(W)$; pick $k_{\text{net}} \in [0.8, 1.6]$ for stress	topology-specific
τ_{ij}	Per-link delay	From RTT or profiling; use queue-free component	0–25 ms

Per-bin conversion uses $\Delta t = 5$ ms. For per-second rates multiply by 200. Defaults are the values used unless stated; sensitivity to $\{\lambda, v_{\text{th}}, \alpha, \kappa\}$ is discussed in this *methods*. Further design and training guidance, including the telemetry pipeline, reset selection, surrogate gradients, and BPTT window choice, is provided in *methods* D.

Table 4: Admissible parameter region used in the experiments. Entries enforce $v \in [0, 1]$, a bin width of 5 ms, and keep the stability condition from Lemma 2 satisfied with margin in operating regimes. Values were sampled within these regions; defaults are given elsewhere for reproducibility.

Parameter	Interpretation	Admissible range (units)
α	excitability scale in f_{sat}	[0.4, 1.0] (dimensionless)
κ	saturation knee of f_{sat}	[0.0, 0.5, 2.0] (dimensionless)
β	linear excitability gain	[-0.10, 0.8] (dimensionless)
γ	constant drive (baseline load)	[0.00, 0.15] (in v units)
λ	service/leak on v	[0.10, 0.30] (per bin ²)
χ	subthreshold damping about v_{rest}	[0.00, 0.08] (per bin)
a	recovery rate	[0.6, 1.8] (per bin)
b	recovery sensitivity to congestion	[0.6, 1.6] (dimensionless)
μ	passive recovery decay	[0.00, 0.35] (per bin)
v_{th}	firing threshold	[0.50, 0.68] (in v units)
k_{reset}	sharpness of reset gate	[10, 20] (dimensionless)
ρ	pullback/reset speed	[3, 8] (per bin)
c	post-event baseline level	[0.0, 0.2] (in v units)
d	recovery jump on event	[0.1, 0.4] (in u units)
I_0	drive offset (arrivals $\rightarrow I$)	[0.08, 0.16] (in v units)
<i>gain</i>	drive scale (arrivals $\rightarrow I$)	[0.8, 1.2] (dimensionless)
τ_s	optional drive smoothing	[0, 15] ms
g	coupling on W (network)	choose so $k_{\text{net}} = g\rho(W) \in [0, 1.8]$
Shot noise	arrival model for synthetic tests	rate $\nu_i \in [10, 50]$ Hz, amplitude $A \in [0.3, 0.9]$
Delays	link propagation	$\tau_{ij} \in [0, 25]$ ms
W normalisation	spectral scaling	$\rho(W) = 1$ before applying g

Exogenous burstiness and measurement noise are included explicitly. We use shot–noise drive as in §?? and allow slow adaptation of tolerance and recovery so the unit becomes temporarily conservative during sustained stress. Concretely, the threshold may wander within a bounded band and the recovery rate may track recent activity

$$v_{\text{th}}(t) = v_{\text{th,base}} + \sigma \xi(t), \quad a(t) = a_0 + \kappa \bar{S}_i(t), \quad (15)$$

where $\xi(t)$ is bounded noise that sets the false–alarm *budget* and $\bar{S}_i(t)$ is the short–window spike (arrival) rate. These adaptations match operator practice such as temporary pacing, token–bucket refill, or ECN–driven headroom.

Training follows standard practice while keeping the networking semantics intact. We employ surrogate gradients at the threshold with a fast–sigmoid derivative

$$\hat{\sigma}'(x) = \frac{1}{(1 + \alpha_{\text{sg}}|x|)^2}, \quad \alpha_{\text{sg}} \approx 5, \quad (16)$$

which keeps gradients finite and centred. To approach crisp events without destabilising optimisation, we use a homotopy on the pullback sharpness k that starts smooth and tightens once optimisation stabilises,

$$\kappa_{\sigma}(t) = \kappa_{\sigma,0} + (\kappa_{\sigma,\text{final}} - \kappa_{\sigma,0}) \min\left\{1, \frac{t}{T_{\text{h}}}\right\}, \quad \kappa_{\sigma,0} \approx 1, \quad \kappa_{\sigma,\text{final}} \in [20, 100]. \quad (17)$$

which preserves gradient quality early and matches event timing late. We also clip gradients by global norm in the range [0.5, 2.0] while k grows. An adaptive optimiser

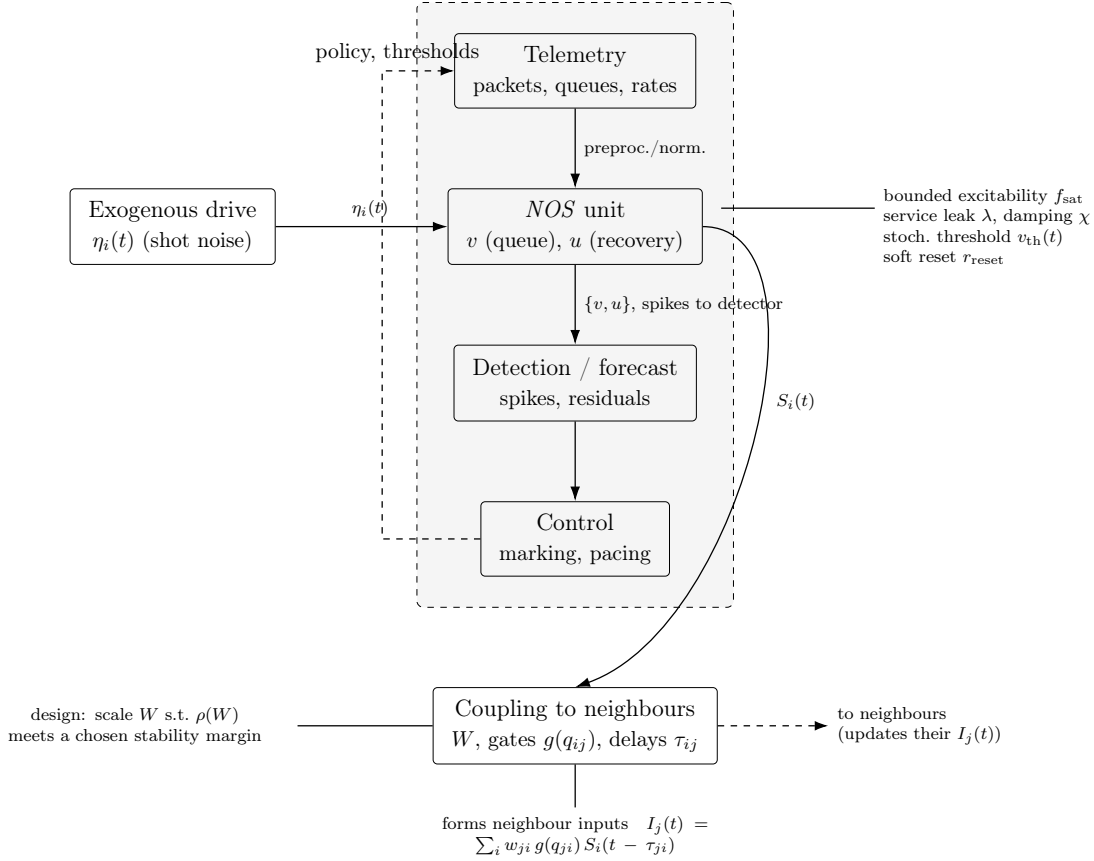


Figure 6: Distributed flow around a *NOS* unit. Telemetry and exogenous shot noise drive the unit. Its state (v, u) feeds detection/control; spikes $S_i(t)$ also propagate to neighbours via weighted, gated, and delayed couplings to form their inputs $I_j(t)$. Control policies feed back to telemetry normalisation (dashed).

such as Adam is suitable; the learning rate is reduced as k increases to maintain stable steps near the threshold. Truncated BPTT should cover the dominant recovery timescale so that u 's memory is learned rather than aliased,

$$T_{\text{BPTT}} \gtrsim \frac{c_*}{a + \mu}, \quad c_* \in [3, 5] \text{ (capturing about 95\%–99\%)}, \quad (18)$$

which aligns with the cool-down used by paced drain or token-bucket refill in devices. After supervised pre-training, slow local updates can be enabled to track diurnal load or policy shifts.

The network view stays explicit. Delays τ_{ij} and gates $g(q_{ij}(t))$ ensure that path timing and residual capacity modulate influence at the right hop and time. The small-signal proxy in (100) makes the stability levers visible to operations: one can lower $\rho(W)$ by reweighting or sparsifying couplings, reduce the global gain g by scheduling, or increase the net drain Λ by raising service λ , damping χ , or recovery a (with b and μ setting trade-offs). These are the same knobs used in practice to keep queues bounded and alerts meaningful, and they connect directly to the analysis that follows.

D.1 Neuromorphic implementation details

Fixed-point state and quantisation. Let (v, u) be stored in $Q_{m.n}$ fixed point with full-buffer scaling V and time base T from (N). The forward map and clipping are

$$v_q = \frac{1}{2^n} \text{clip}\left(\text{round}\left(\frac{v}{V} 2^n\right), 0, 2^m - 1\right), \quad u_q = \frac{1}{2^n} \text{clip}\left(\text{round}\left(\frac{u}{V} 2^n\right), 0, 2^m - 1\right). \quad (19)$$

With this scaling, $\tilde{v} \in [0, 1]$ remains interpretable as normalised queue level; overflow is prevented by the saturation in f_{sat} .

Discrete-time soft reset. On digital substrates the exponential reset (27) is applied per tick Δt only when a spike occurs. Let \tilde{v}_{t+1} denote the state after the continuous update but before any reset. Then

$$v_{t+1} = (1 - S_i(t)) \tilde{v}_{t+1} + S_i(t) \left[c + (\tilde{v}_{t+1} - c) e^{-r_{\text{reset}} \Delta t} \right], \quad (20)$$

$$u_{t+1} = u_t + d S_i(t), \quad (21)$$

where $S_i(t) \in \{0, 1\}$ indicates a threshold crossing (a spike) at time t for neuron i . The factor $e^{-r_{\text{reset}} \Delta t}$ is realised by a multiply-accumulate or by a bit-shift if $r_{\text{reset}} \Delta t$ is drawn from a small table.

Logistic pullback via LUT or PWL. The continuous pullback (28) uses $\sigma_{\kappa_\sigma}(x) = 1/(1 + e^{-\kappa_\sigma x})$. On hardware we use a lookup table or piecewise-linear approximation $\hat{\sigma}_{\kappa_\sigma}$ on a bounded interval $x \in [-x_{\text{max}}, x_{\text{max}}]$:

$$|\sigma_{\kappa_\sigma}(x) - \hat{\sigma}_{\kappa_\sigma}(x)| \leq \varepsilon_{\text{LUT}} \quad \text{for } |x| \leq x_{\text{max}}. \quad (22)$$

The induced drift error on the pullback term is then bounded by $r_{\text{reset}} |v - c| \varepsilon_{\text{LUT}}$ and can be kept below a configured fraction of the net drain in (99).

Graph coupling, delays, and AER routing. Sparse coupling $W = [w_{ij}]$ is realised by address-event routing tables; per-link delays are integer tick buffers

$$\tilde{\tau}_{ij} = \text{round}\left(\frac{\tau_{ij}}{T}\right) \in \mathbb{N}, \quad (23)$$

which preserves the causality of (6). Gates $g(q_{ij})$ are evaluated where the link queue state is maintained; their outputs modulate the synaptic multiplier before accumulation.

Fabric-rate and budget constraints. Let R_{max} be the sustainable spike throughput per core and let \bar{r}_j be the observed rate of S_j . A conservative admission constraint that avoids router overload is

$$\sum_j \mathbf{1}\{w_{ij} \neq 0\} \bar{r}_j \leq R_{\text{max}} \quad \text{for each core hosting neuron } i, \quad (24)$$

or, in matrix form for a deployment-wide check, $\|W\|_{0,1} \bar{r}_{\text{max}} \leq R_{\text{max}}$, where $\|W\|_{0,1}$ counts nonzeros per row and $\bar{r}_{\text{max}} = \max_j \bar{r}_j$.

Operational margin under quantisation. Let Δ_{net} be the margin in (101). Finite precision induces errors in $f'_{\text{sat}}(v^*)$, in W , and in gains. If $\delta_{f'}$, δ_W , and δ_g bound these relative errors, then a sufficient robustness condition is

$$\Delta_{\text{net}} > g \rho(W) f'_{\text{sat}}(v^*) (\delta_{f'} + \delta_W + \delta_g) + \varepsilon_{\text{LUT}} \rho \mathbb{E}\{|v - c|\}, \quad (25)$$

which ensures that the stability proxy (100) still holds after rounding and table approximations.

Networking alignment and reporting. Choose (V, T) so that V matches the full-buffer level used by the QoS policy and T matches the scheduler epoch or drain time. Report energy per spike and energy per detection alongside CPU baselines, and log $\tilde{\tau}_{ij}$ histograms to confirm that delay quantisation preserves path ordering. These checks keep the deployed *NOS* consistent with the queueing semantics and timing used in the main text.

E Spike generation and resets

Two differentiable reset strategies are introduced, an event-triggered exponential soft reset and a continuous pullback shaped by a sigmoid, both enabling gradient-based training while preserving spiking dynamics. A spike indicates that the local congestion proxy exceeded tolerance and triggers a control action such as ECN marking, rate reduction, or an alert to the controller. To reflect tolerance bands and measurement noise we allow a stochastic threshold with bounded dispersion:

$$v_i(t) \geq v_{\text{th}}(t) = v_{\text{th,base}} + \sigma \xi(t), \quad (26)$$

where $\xi(t)$ is zero-mean, bounded (e.g., clipped Gaussian or uniform), and σ is tuned to the false-alarm budget on residuals. This construction separates policy (the base threshold) from instrumentation noise (the dispersion).

Event-based exponential soft reset. Right after a threshold crossing, the unit should return toward a baseline without a hard discontinuity. For a forward-Euler step of size Δt we apply

$$v_i \leftarrow c + (v_i - c) e^{-r_{\text{reset}} \Delta t}, \quad u_i \leftarrow u_i + d, \quad (27)$$

which makes v_i relax exponentially toward c with rate r_{reset} and increments u_i by d to encode refractory depth. In networking terms, (27) models a paced drain after a trigger together with a short-lived slow-down in effective send or admit rate. The pair (r_{reset}, d) is set from post-burst relaxation fits on v and the desired “cool-down” depth in u .

Continuous differentiable pullback. Alternatively, we add to the v -dynamics in (2) a smooth term that engages only above threshold:

$$-r_{\text{reset}} \sigma_{\kappa\sigma}(v_i - v_{\text{th}}(t)) (v_i - c), \quad \sigma_{\kappa\sigma}(x) = \frac{1}{1 + e^{-\kappa\sigma x}}, \quad r_{\text{reset}} > 0. \quad (28)$$

For $v_i < v_{\text{th}}(t)$ the multiplier $\sigma_{\kappa\sigma}$ is near 0 and the pullback is negligible. Once v_i exceeds the threshold, $\sigma_{\kappa\sigma}$ rises toward 1 and an exponential attraction to c turns on as

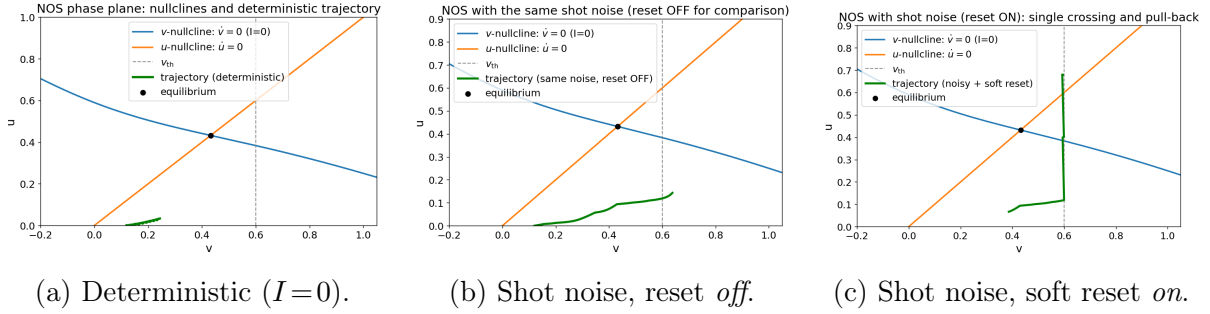


Figure 7: NOS phase–plane diagnostics with nullclines $\dot{v} = 0$ and $\dot{u} = 0$, threshold v_{th} , equilibrium, and short trajectories. **(a)** Baseline geometry: the parabolic v -nullcline intersects the linear u -nullcline at a stable equilibrium; the threshold sits to the right. **(b)** With identical exogenous shot noise but reset disabled, the trajectory creeps toward the threshold and remains above the u -nullcline, indicating slow accumulation of *effective* load that can lead to prolonged excursions. **(c)** With the same noise and the exponential soft reset active, the trajectory crosses the threshold once, is immediately pulled back toward c , and rises in u , which encodes a temporary conservative phase. Operationally, panel (c) mirrors paced drain after an alarm: timing is preserved by the threshold crossing, the return to baseline follows the configured time scale r_{reset}^{-1} , and the recovery increment d captures the short-lived send-rate reduction.

a continuous part of \dot{v} . Training proceeds with a homotopy in κ_{σ} , starting smooth and sharpening as optimisation stabilises, which preserves gradient quality while converging to crisp event timing. For reference, the nullclines of the no–input skeleton are

$$\dot{v} = 0 : u = f_{\text{sat}}(v) + (\beta - \lambda - \chi)v + \gamma + \chi v_{\text{rest}}, \quad (29)$$

$$\dot{u} = 0 : u = \frac{ab}{a + \mu} v \quad (30)$$

Figure 7 clarifies the role of the smooth pullback in a networking setting. In panel 7a the skeleton geometry is benign: the parabolic v -nullcline (29) meets the linear u -nullcline (30) at a stable point well to the left of the threshold. In panel 7b, identical shot–noise drive nudges v upward but, with the reset disabled, there is no restoring action triggered at the moment of crossing; the trajectory can linger near v_{th} , which in practice sustains high send pressure on downstream links. In panel 7c, the same bursts cause a single threshold crossing followed by an immediate, continuous return toward c . The concurrent rise in u encodes a short conservative phase, matching paced drain or token–bucket refill after an alarm. Because (28) is differentiable, these operator–visible effects are trainable: r_{reset}^{-1} is tuned to device drain time or scheduler epoch, c to the desired post–event baseline, and d to the depth of temporary slow–down. The model therefore reproduces both the timing of decisions and the engineered cool–down that follows, without introducing discontinuities that harm gradient–based learning or blur attribution.

F Local slope bounds and saturation properties

For convenience we collect here the elementary properties of the bounded excitability function

$$f_{\text{sat}}(v) = \frac{\alpha v^2}{1 + \kappa v^2}, \quad \alpha > 0, \kappa > 0, \quad (5 \text{ revisited})$$

used in Section 2.3. These properties underpin the existence and uniqueness conditions for the subthreshold equilibrium and the small-signal stability margins.

We first record its small-signal expansion and limiting value:

$$f_{\text{sat}}(v) \sim \alpha v^2 \quad \text{as } v \rightarrow 0, \quad (31)$$

and enforces a finite ceiling for heavy load, ensuring bounded behaviour

$$\lim_{v \rightarrow \infty} f_{\text{sat}}(v) = \frac{\alpha}{\kappa}. \quad (32)$$

The derivative is globally bounded, which improves numerical stability and yields clean gain conditions, which means, it recovers a quadratic slope for small v while enforcing saturation for large v :

$$f'_{\text{sat}}(v) = \frac{2\alpha v}{(1 + \kappa v^2)^2}, \quad (33)$$

is globally bounded, with maximum

$$\max_v f'_{\text{sat}}(v) = \frac{3\sqrt{3}}{8} \frac{\alpha}{\sqrt{\kappa}} \quad \text{at } v = \frac{1}{\sqrt{3\kappa}}. \quad (34)$$

The quantity in (34) is the steepest admissible local growth of the excitability term and appears in the service-dominance inequalities used for equilibrium uniqueness and Jacobian stability tests.

The consequences of this bounded excitability under stochastic drive are examined in *methods* G and G.1.

G Noise sensitivity under stochastic drive

We model arrivals as shot noise with exponential smoothing. For node i ,

$$\eta_i(t) = \sum_{n=1}^{N_i(t)} A_{i,n} e^{-(t-t_{i,n})/\tau_s} H(t - t_{i,n}), \quad N_i(t) \sim \text{Poisson}(\nu_i t), \quad (35)$$

where ν_i is the event rate, $A_{i,n}$ are i.i.d. amplitudes, τ_s is a smoothing time, and H is the Heaviside step. The process is stationary with mean, variance, and autocovariance

$$\mathbb{E}[\eta_i] = \nu_i \mathbb{E}[A_i] \tau_s, \quad \text{Var}[\eta_i] = \nu_i \mathbb{E}[A_i^2] \frac{\tau_s}{2}, \quad \text{Cov}_{\eta_i}(\tau) = \nu_i \mathbb{E}[A_i^2] \frac{\tau_s}{2} e^{-|\tau|/\tau_s}. \quad (36)$$

Its power spectrum is Lorentzian,

$$S_{\eta_i}(\omega) = \frac{2 \nu_i \mathbb{E}[A_i^2] \tau_s}{1 + \omega^2 \tau_s^2}. \quad (37)$$

In networking terms, $(\nu_i, \mathbb{E}[A_i], \tau_s)$ are read from the same counters and windows used in telemetry: ν_i is the burst-start rate, $\mathbb{E}[A_i]$ is the mean per-burst mass after smoothing, and τ_s matches the prefilter that removes counter jitter while preserving micro-bursts.

Small-signal sensitivity. Linearising *NOS* at a subthreshold equilibrium (v^*, u^*) with $\bar{d} = f'_{\text{sat}}(v^*) + \beta - \lambda - \chi$ gives

$$\begin{aligned} \frac{d}{dt} \begin{bmatrix} \delta v \\ \delta u \end{bmatrix} &= \begin{bmatrix} \bar{d} & -1 \\ ab & -(a + \mu) \end{bmatrix} \begin{bmatrix} \delta v \\ \delta u \end{bmatrix} + \begin{bmatrix} 1 \\ 0 \end{bmatrix} \eta_i(t), \\ H_v(s) &= \frac{\delta V(s)}{E(s)} = \frac{s + (a + \mu)}{(s - \bar{d})(s + (a + \mu)) + ab}. \end{aligned} \quad (38)$$

The DC gain and the variance of δv under (37) are

$$H_v(0) = \frac{a + \mu}{ab - (a + \mu)\bar{d}}, \quad \sigma_v^2 = \frac{1}{2\pi} \int_{-\infty}^{\infty} |H_v(i\omega)|^2 S_{\eta_i}(\omega) d\omega. \quad (39)$$

As the node approaches its local margin ($ab \downarrow (a + \mu)\bar{d}$) or the network approaches the Perron-mode threshold ($k \rightarrow k^*$), $|H_v(0)|$ increases and the integral in (39) grows, so the same shot-noise trace produces larger queue excursions and more threshold crossings.

Firing statistics and cascades. We summarise sensitivity by the mean firing rate \bar{f} , the inter-spike-interval coefficient of variation (CV), and avalanche sizes S (contiguous above-threshold activity aggregated over neighbours). With parameters fixed and only the noise amplitude varied, three robust effects appear, consistent with (38)–(39) and bounded excitability: (i) \bar{f} rises with amplitude in all regimes, with a steeper slope near the coupling threshold because small increments in η_i map to larger δv ; (ii) CV increases near threshold, reflecting irregular, burst-dominated spike trains as variance grows; (iii) the tail of $P(S)$ becomes heavier with amplitude, indicating extended congestion cascades when fluctuations push multiple nodes above threshold before recovery completes.

Networking interpretation. Higher ν_i or larger $\mathbb{E}[A_i^2]$ means burstier ingress; increasing τ_s models longer burst coherence. The levers that reduce noise sensitivity are the same that enlarge deterministic headroom: higher service and subthreshold damping (λ, χ), faster recovery ($a + \mu$), and earlier saturation (larger κ , which lowers $f'_{\text{sat}}(v^*)$ and hence \bar{d}). Each reduces $H_v(0)$ and the variance integral in (39). With per-link gates, attenuating w_{ij} on noisy edges reduces the effective drive entering I_i and moves the network away from the Perron threshold.

Empirical summary (Fig. 8). The rate curves show \bar{f} versus amplitude A for subcritical ($k = 0.9$) and near-threshold ($k = 1.36$) regimes; the steeper slope near $k = 1.4$ matches the growth of $|H_v(0)|$. The CV curves increase with A and peak near threshold, consistent with (39). The avalanche distributions broaden as A increases; heavier tails near $k \approx k^*$ reflect larger correlated excursions. These trends are stable across $\rho_s \in \{10, 20, 50\}$ Hz and the reported τ_s range, and they align with the linear response in (38). Further quantitative tail fits are provided below in G.1.

G.1 Statistical robustness under noise

For each condition we estimated the mean firing rate \bar{f} and the inter-spike-interval coefficient of variation (CV) using non-parametric bootstrap resampling (hundreds of replicates). Bootstrap 95% intervals show that both \bar{f} and CV increase with shot-noise

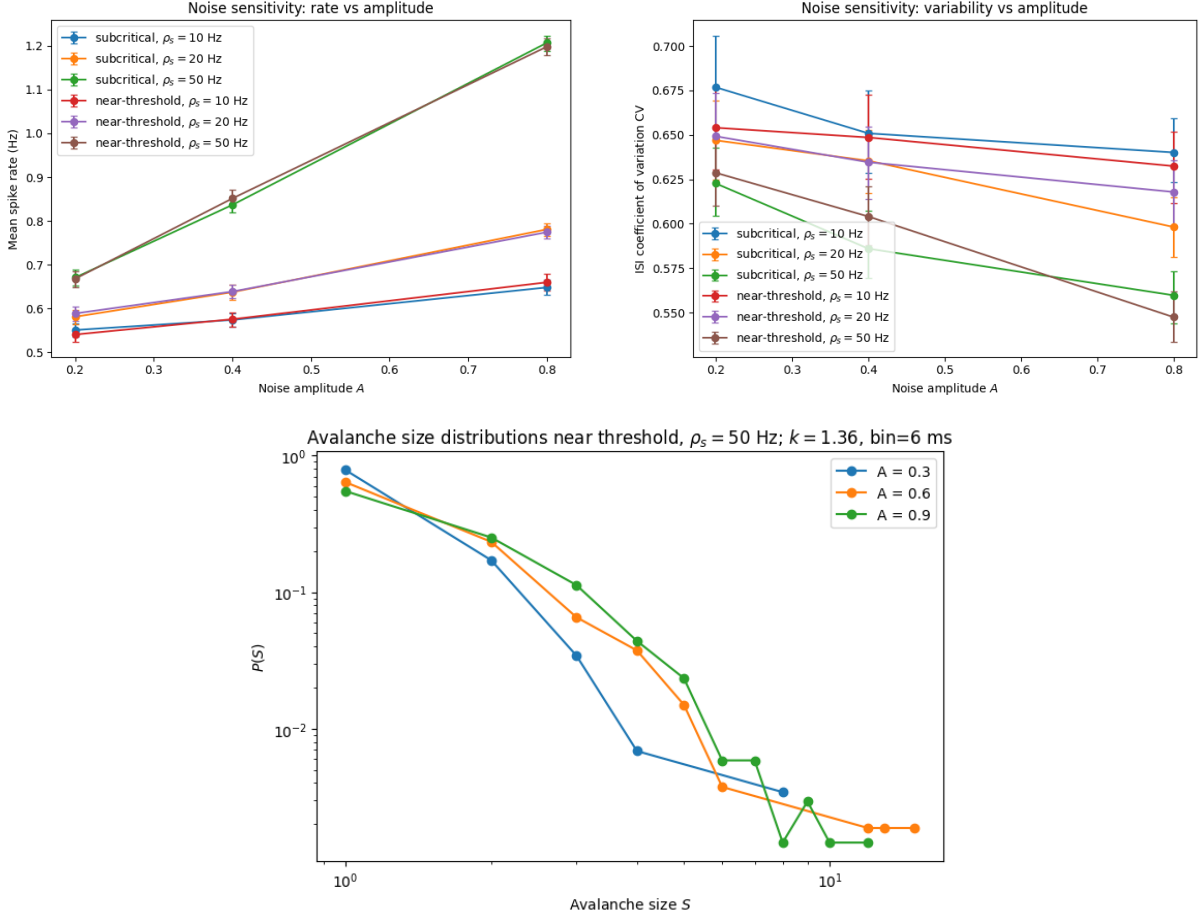


Figure 8: Noise sensitivity in *NOS*. (**Top left**) Mean firing rate \bar{f} versus amplitude A for subcritical ($k = 0.9$) and near-threshold ($k = 1.36$) regimes at $\rho_s \in \{10, 20, 50\}$ Hz. (**Top right**) Inter-spoke interval CV versus A under the same conditions. Error bars show bootstrap 95% confidence intervals. (**Bottom**) Avalanche size distributions $P(S)$ near threshold ($k = 1.36$, $\rho_s = 50$ Hz). Heavier tails appear as A increases, corresponding to extended cascades.

amplitude A , particularly near threshold. In *NOS*, stronger stochastic drive raises overall excitability and increases irregularity, mirroring more variable queue dynamics.

Avalanche size distributions $P(S)$ were then analysed. Figure 9 shows empirical complementary cumulative distributions with fitted power-law and log-normal overlays above a data-driven tail threshold x_{\min} . Tail parameters were estimated by maximum likelihood with truncation at x_{\min} ; goodness was assessed by the Kolmogorov–Smirnov distance and model choice by AIC. Across conditions, AIC favours the power-law, indicating scale-free-like behaviour near threshold. Fitted values are reported in Table S5.

The exponents display a clear trend: at low amplitude ($A = 0.3$) the power-law exponent is $\hat{\alpha} \approx 8.7$ (steep decay, small avalanches). At $A = 0.6$ the exponent decreases to $\hat{\alpha} \approx 6.4$ (broader tail). At $A = 0.9$ the exponent drops to $\hat{\alpha} \approx 3.3$ (heavy tail and a higher chance of large cascades). Thus, near the bifurcation, stronger stochastic drive allows small fluctuations to trigger system-wide congestion events.

Avalanche definition and fitting. Avalanche sizes S were computed from population spike counts in 5 ms bins (the experimental Δt): an avalanche is a contiguous run of

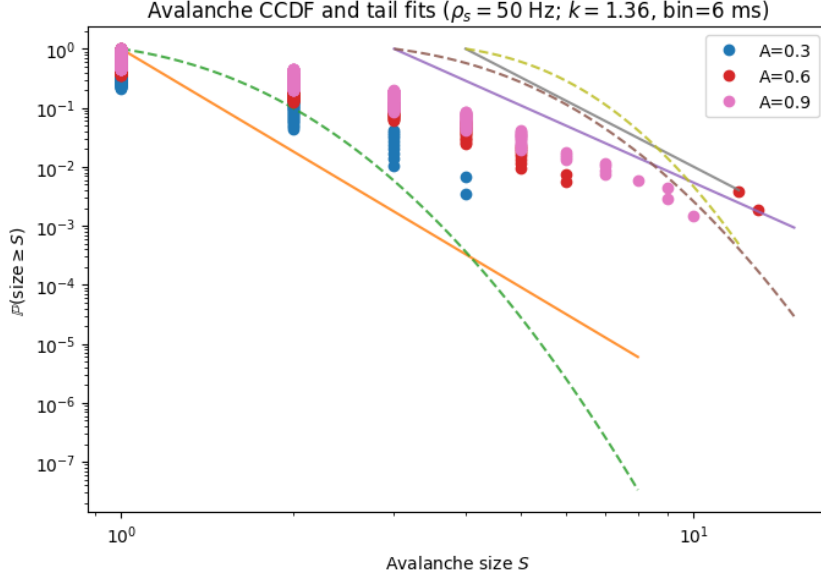


Figure 9: Avalanche complementary CDFs near threshold ($k = 1.36$, $\rho_s = 50$ Hz). Empirical distributions (points) with fitted power-law (solid) and log-normal (dashed) overlays above the estimated x_{\min} for each amplitude A . Model selection used AIC; numerical results appear in Table S5.

Table 5: Avalanche tail fits near threshold ($k = 1.36$, $\rho_s = 50$ Hz). For each amplitude A , we report the tail threshold x_{\min} , tail size n , maximum-likelihood parameters, KS distance (for the truncated tail), log-likelihood (LL), AIC, and the preferred model.

A	x_{\min}^{PL}	n_{PL}	$\hat{\alpha}$	KS_{PL}	LL_{PL}	AIC_{PL}	x_{\min}^{LN}	n_{LN}	$\hat{\mu}$	$\hat{\sigma}$	KS_{LN}	LL_{LN}	AIC_{LN}	Pref.
0.3	2.0	63	8.73	0.76	14.03	-26.07	2.0	63	0.82	0.27	0.76	-34.20	72.39	PL
0.6	4.0	31	6.43	0.58	-27.24	56.48	4.0	31	1.57	0.31	0.58	-46.15	96.31	PL
0.9	1.0	681	3.25	0.53	-431.13	864.26	1.0	681	0.44	0.53	0.53	-684.68	1373.35	PL

nonzero bins, with size equal to the total spikes in the run. For each condition, x_{\min} minimised the KS distance between empirical and model CDFs (tail only). Power-law tails used the continuous-tail MLE $\hat{\alpha} = 1 + n / \sum_{i=1}^n \log(x_i/x_{\min})$ with model $F(x) = 1 - (x/x_{\min})^{1-\hat{\alpha}}$ for $x \geq x_{\min}$. Log-normal tails were fit by MLE on $\log x$ with truncation at x_{\min} . Model selection used AIC with parameter counts 1 (power-law) and 2 (log-normal).

H Queueing baseline comparison

Experimental setup. We compare *NOS* against canonical queueing baselines in two modes. (i) **Open-loop:** we drive M/M/1 (analytic mean, $\rho < 1$), simulated M/M/1/ K , and a single *NOS* unit with *the same* exogenous arrivals and report observables in the *same unit* (packets). Light-load calibration aligns means: we choose an input gain and output scale so that the *NOS* mean at small ρ matches the M/M/1 mean $\mathbb{E}[L] = \rho/(1-\rho)$. Tail behaviour is then tested under a common MMPP burst sequence (same ON/OFF epochs), which is the operational regime of interest. (ii) **Closed-loop:** we attach three controllers to the same offered-load trace and compare the resulting queue trajectories

and marking signals $p(t)$: A) NOS-based (marking derived from *NOS* subthreshold state with soft reset), B) *queue* controller (marking from the raw queue), and C) *LP-queue* controller (marking from a lightly low-pass filtered queue). All three use the same logistic nonlinearity for $p(t)$ so differences are due to the state fed to the nonlinearity.

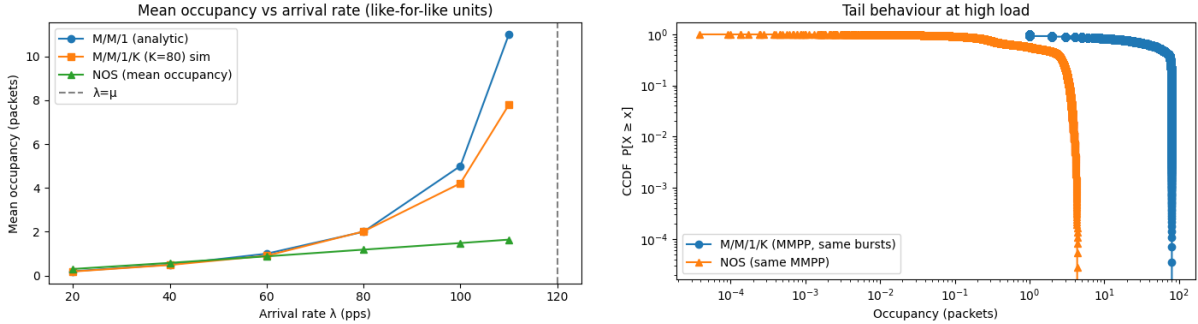


Figure 10: Open-loop comparisons in packet units. **(Left)** Mean occupancy versus arrival rate λ_{arr} : M/M/1 (analytic, $\rho < 1$), simulated M/M/1/K, and *NOS* (calibrated at light load). *NOS* bends earlier near saturation due to bounded excitability and soft reset. **(Right)** Tail CCDF under a common MMPP burst sequence: M/M/1/K displays a slow tail, whereas *NOS* truncates cascades via continuous pull-back, yielding a much lighter tail.

How to read the open-loop panels (networking view). Figure 10 (left) shows mean occupancy versus arrival rate λ_{arr} with a fixed service μ_{srv} . The blue curve (M/M/1) is the textbook reference that diverges as $\rho = \lambda_{\text{arr}}/\mu_{\text{srv}} \uparrow 1$. The orange curve (M/M/1/K) follows M/M/1 until blocking becomes material. The green curve (*NOS*) rises with load at small ρ (by calibration) but *bends earlier* as ρ grows; bounded excitability and continuous pull-back reduce the subthreshold slope and drain excursions. Operationally, this mirrors how modern AQMs aim to keep average queues low near saturation rather than letting them diverge smoothly.

Figure 10 (right) plots the complementary CDFs of occupancy under the *same* MMPP burst sequence. M/M/1/K develops a long tail during ON periods (large probability of deep queues), whereas *NOS* exhibits a much sharper tail because soft reset and leak truncate cascades. In networking terms, *NOS* converts the same burst train into fewer deep-queue events—directly improving tail latency and reducing drop/mark storms. The aggressiveness of this truncation is tunable through the subthreshold leak χ , the reset rate r_{reset} , and the saturation knee κ ; operators can place the tail against SLO targets (e.g., $\mathbb{P}\{Q \geq q_0\} \leq \varepsilon$).

How to read the closed-loop panels (networking view). Figure 11 contrasts three marking strategies under the same offered-load traces. The top panel shows controller outputs $p(t)$. *NOS* (blue) is decisive and low-jitter; the queue controller (orange) is noisy (mark jitter follows queue noise); the LP-queue controller (green) is smoother but lags, so it reacts late to bursts. The middle panel shows a step in offered load: *NOS* snaps to target with minimal ringing; the queue controller oscillates; the LP-queue controller overshoots and then settles slowly. The bottom panel shows a burst train: *NOS* produces short, clipped spikes; the queue controller shows noisy peaks; the LP-queue controller permits taller spikes because filtering delays the reaction. Practically, *NOS*

shrinks the time spent at high queue levels and reduces burst amplification without a long averaging window, which improves tail latency and fairness while avoiding prolonged ECN saturation.

Summary for operators. The baselines anchor *NOS* against established theory. When the objective is to *match the classical infinite-buffer mean* at light load, M/M/1 gives the right reference and *NOS* can be calibrated to agree. When the objective is to *manage burst risk and stability* under finite resources and coupling, *NOS*' bounded excitability and differentiable pull-back are strictly more faithful: they reduce deep-queue probability, yield crisper ECN/markings, and shorten congestion episodes without heavy filtering. The same knobs that appear in our stability proxies— χ , λ_{arr} -like drain, κ , and reset parameters—map directly to deployed policy controls (AQM leak, scheduler epoch, ramp shaping, and post-alarm conservatism), making the model both predictive and actionable. Having established mechanistic fidelity and control behaviour, we next ask how *NOS* fares as a label-free forecaster against compact ML/SNN baselines.

I Stochastic arrivals: shot noise model and calibration

Network arrivals are bursty, short-correlated within flows, and heavy-tailed across flows. To expose this variability to the model while staying compatible with measurement practice, we represent exogenous drive at node i by a compound Poisson shot-noise process smoothed at an operator-chosen time scale:

$$\eta_i(t) = \sum_{n=1}^{N_i(t)} A_{i,n} \kappa_s(t - t_{i,n}), \quad (40)$$

where $N_i(t)$ is a Poisson process of rate ν_i , the amplitudes $A_{i,n}$ reflect burst size, and κ_s is a causal exponential smoothing kernel such as

$$\kappa_s(t) = e^{-t/\tau_s} H(t), \quad (41)$$

$$H(t) = \begin{cases} 0, & t < 0, \\ 1, & t \geq 0, \end{cases} \quad (42)$$

so $H(t)$ enforces causality (no effect before the burst) and the factor e^{-t/τ_s} sets an exponential decay with time scale τ_s (the burst's influence fades smoothly). When needed, a normalised variant keeps unit area:

$$\kappa_s^{\text{norm}}(t) = \frac{1}{\tau_s} e^{-t/\tau_s} H(t). \quad (43)$$

The normalisation is set so that $A/(v_{\text{th}} - v_{\text{rest}})$ falls in a practical range for the workload. This construction aligns with the EWMA-style smoothing used in telemetry pipelines and permits direct calibration from packet counters.

Equation (40) mirrors the way operators pre-process packet counters and flow logs: arrivals are bucketed, lightly smoothed, and scaled. The rate ν_i matches the observed burst-start rate at node i over the binning interval; the amplitude $A_{i,n}$ matches per-burst byte or packet mass after the same smoothing; and τ_s is set to the shortest window that suppresses counter jitter without hiding micro-bursts. The normalisation is chosen so

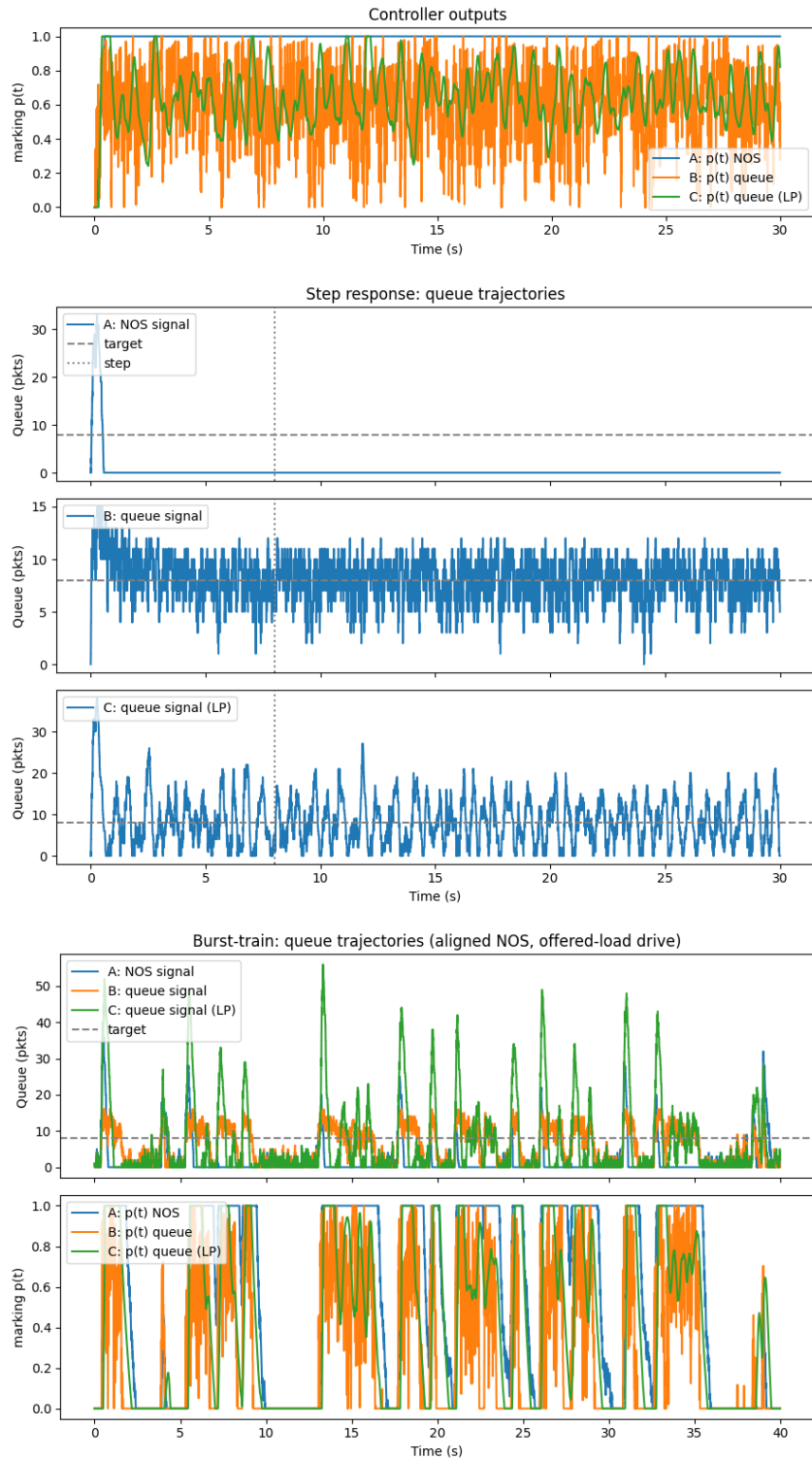


Figure 11: Closed-loop behaviour under identical offered-load traces. **(Top)** Marking signals $p(t)$ from three controllers: *NOS* (blue), raw queue (orange), and low-pass filtered queue (green). **(Middle)** Step response: *NOS* returns to target fastest with little ringing; queue-only is jitter-dominated; LP-queue trades jitter for lag and overshoot. **(Bottom)** Burst train: *NOS* clips spikes and shortens congestion episodes; queue-only is noisy; LP-queue allows taller spikes due to filter delay.

that a single exogenous shot changes v by a fraction ϵ of the threshold margin $m = v_{\text{th}} - v_{\text{rest}}$, with $\epsilon \in [10^{-3}, 2 \times 10^{-1}]$. The lower bound clears telemetry noise; the upper bound prevents a single burst from forcing a reset. In discrete time this corresponds to $A \Delta t / m \in [10^{-3}, 2 \times 10^{-1}]$; under the exponential kernel $\kappa_s(t) = e^{-t/\tau_s} H(t)$ it corresponds to $A \tau_s / m \in [10^{-3}, 2 \times 10^{-1}]$. Using (40) inside $I_i(t)$ in (1) makes the event drive consistent with the graph structure and delays defined in (6). In effect, traffic statistics enter *NOS* with the same time base and smoothing that appear in the telemetry pipeline, which simplifies both training and post-deployment troubleshooting.

J Delayed gates and per-link queues

When links maintain their own queues, we gate the coupling by a per-link occupancy $q_{ij}(t)$. A simple queue-level description is

$$\dot{q}_{ij} = -\zeta q_{ij} + \Phi(S_j(t)) - \Psi(q_{ij}), \quad (44)$$

and we replace $w_{ij} S_j(t - \tau_{ij})$ by $w_{ij} g(q_{ij}) S_j(t - \tau_{ij})$. This produces a two-layer representation: node integrator plus per-link capacity gating. Here Φ maps presynaptic activity to arrivals on ($j \rightarrow i$), Ψ represents service or RED/ECN-like bleed, and g is a bounded, monotone gate that reduces influence when the link is loaded. This separates phenomena cleanly: node excitability remains interpretable in queue units, while link congestion only modulates the strength and timing of coupling.

Per-link queue gating (dimensionally explicit). Let $q_{ij}(t)$ denote the normalised occupancy of link (i, j), with $q_{ij} \in [0, 1]$. Choose a single time constant $\tau_q > 0$ and a bounded, dimensionless encoding $\sigma_s : \mathbb{R} \rightarrow [0, 1]$ of the presynaptic drive $S_j(t)$. We model the queue as a leaky accumulator of arrivals:

$$\tau_q \dot{q}_{ij}(t) = -q_{ij}(t) + \sigma_s(S_j(t)), \quad (45)$$

so that $[\tau_q] = \text{time}$ and q_{ij} is dimensionless. The effective coupling is then

$$w_{ij}^{\text{eff}}(t) = w_{ij} g(q_{ij}(t)), \quad g : [0, 1] \rightarrow [0, 1], \quad (46)$$

with gates such as

$$g(x) = (1 - x)^p \quad (\text{capacity fade, } p > 1), \quad (47)$$

$$g(x) = \frac{1}{1 + \exp\{k(x - \theta)\}} \quad (\text{logistic gate}). \quad (48)$$

One then replaces $w_{ij} S_j(t - \tau_{ij})$ in (6) by $w_{ij}^{\text{eff}}(t) S_j(t - \tau_{ij})$. This cleanly separates node adaptation from link capacity effects. In practice it lets an operator disclose where instability originates: node excitability, link queues, or topology. For completeness, the original form (44) is dimensionally consistent provided $[\zeta] = \text{time}^{-1}$ and $[\Phi(S)] = [\Psi(q)] = \text{time}^{-1}$; (45) corresponds to the special case $\zeta = \tau_q^{-1}$, $\Phi(S) = \tau_q^{-1} \sigma_s(S)$, and $\Psi \equiv 0$.

Networking interpretation and design guidance. Equation (6) enforces hop-level causality: bursts from j affect i only after τ_{ij} , so back-pressure and wavefront effects appear on the correct timescale. The queue model in (44)–(45) captures how a busy uplink or radio fades coupling without requiring packet loss. The drain term Ψ can represent ECN or token-bucket service, while the gate $g(\cdot)$ reduces the effective link weight as occupancy rises. The power gate in (47) suits wired interfaces where capacity fades smoothly with load. The logistic gate in (48) matches thresholded policies such as priority drops, wireless duty cycling, or scheduler headroom rules. Because $w_{ij}^{\text{eff}}(t)$ multiplies $S_j(t - \tau_{ij})$ in (6), congestion localises: only the affected links attenuate, which keeps attribution simple in operations dashboards.

Calibration follows telemetry. Choose τ_{ij} from the queue-free component of RTT. Set τ_q near the interface drain time or the QoS smoothing window. Normalise w_{ij} by nominal link rates or policy priorities, then scale $W = \{w_{ij}\}$ so its spectral radius meets the desired small-signal index; under stress the gate g reduces the effective spectral radius, enlarging the stable operating region. In evaluation, this decomposition helps explain behaviour: if instability appears with empty q_{ij} the cause is node excitability or topology; if it vanishes when g engages, the bottleneck is link capacity or scheduling.

J.1 Delayed events and per-link gates in practice

This note elaborates on the roles of τ_{ij} and $g(q_{ij}(t))$ in (6) and (45).

Timing. The shift $S_j(t - \tau_{ij})$ represents propagation and processing delay on (j, i) . It aligns presynaptic events with the time packets reach node i . Delay changes phase in closed loops, which affects stability margins and the onset of oscillations.

Conditioning. The gate $g(q_{ij}(t))$ encodes a per-link condition such as residual capacity, scheduler priority, or queue occupancy. As q_{ij} grows, the effective weight $w_{ij}^{\text{eff}}(t) = w_{ij}g(q_{ij}(t))$ shrinks, so a congested link contributes less drive downstream. This mimics policing, AQM, or rate limiting and prevents the model from reinforcing overloaded paths.

Examples.

- *Datacentre incast.* Multiple senders j spike toward a top-of-rack switch i . Per-link queues q_{ij} rise, $g(q_{ij})$ falls, and w_{ij}^{eff} shrinks, so $I_i(t)$ reflects effective rather than nominal bandwidth.
- *WAN hop with high delay.* A large τ_{ij} shifts S_j by tens of milliseconds. The delayed drive prevents premature reactions at i and yields a stability test that depends on both $\rho(W)$ and the phase introduced by τ_{ij} .
- *Wireless fading.* Treat short-term SNR loss as a temporary rise in q_{ij} or as a change in the gate parameters. The same S_j then has smaller impact at i , consistent with link adaptation that lowers the offered load.

Operator workflow. Use passive RTT sampling or active probes to estimate τ_{ij} . Fit τ_q to the decay of q_{ij} when input drops or to the effective averaging window of the QoS policy. Set w_{ij} proportional to nominal capacity or administrative weight, then scale W to the target small-signal index. Validate g by replaying traces with known congestion episodes and checking that w_{ij}^{eff} attenuates the expected links while leaving others unchanged.

K Equilibrium and stability: detailed derivations

K.1 Equilibrium equations (derivations)

For node i , let (v_i^*, u_i^*) denote a subthreshold equilibrium ($\dot{v}_i = \dot{u}_i = 0$). At such a steady state, the (3) implies a linear relation between recovery and queue level:

$$u_i^* = \frac{ab}{a + \mu} v_i^*. \quad (49)$$

Substituting (49) into (2) gives

$$0 = f_{\text{sat}}(v_i^*) + (\beta - \lambda - \chi) v_i^* + \gamma + \chi v_{\text{rest}} - u_i^* + I_i^*, \quad (50)$$

where I_i^* denotes the long-run mean of the graph-local drive at node i (including delayed contributions). Eliminating u_i^* yields a scalar fixed-point equation for v_i^* :

$$f_{\text{sat}}(v_i^*) + \left(\beta - \lambda - \chi - \frac{ab}{a + \mu} \right) v_i^* + \gamma + \chi v_{\text{rest}} + I_i^* = 0. \quad (51)$$

Equation (51) balances three effects: a convex rise with load through f_{sat} , linear drain through the net service and damping, and the constant baseline from $\gamma + \chi v_{\text{rest}} + I_i^*$. The mean input I_i^* aggregates neighbour activity over the network with delays; under stationary traffic it is well defined because the delayed sum in (6) averages to a constant.

Quadratic small-signal approximation. For analytic visibility, replace $f_{\text{sat}}(v) \approx \alpha v^2$ in a small-signal regime and define

$$L := \beta - \lambda - \chi - \frac{ab}{a + \mu}, \quad C := \gamma + \chi v_{\text{rest}} + I_i^*. \quad (52)$$

Then (51) reduces to

$$\alpha(v_i^*)^2 + L v_i^* + C = 0, \quad (53)$$

with discriminant

$$D_i = L^2 - 4\alpha C. \quad (54)$$

If $D_i \geq 0$ and the admissible root lies in $[0, 1]$, it approximates v_i^* and clarifies how the operating point moves with C . In networks, service and damping must outpace the steepest small-signal gain of f_{sat} ; the corollary in M provided a direct algebraic check. In the quadratic approximation, the sign of D_i in (54) separates three regimes: $D_i < 0$ (no real root, parameter mismatch), $D_i = 0$ (tangent balance at a single v_i^*), and $D_i > 0$ (two mathematical roots, of which the physically admissible one lies in the queue range and satisfies the stability test below).

Existence and uniqueness on $[0, 1]$. The monotonicity criterion introduced earlier applies with L as in (52): a sufficiently positive net slope $f'_{\text{sat}}(v) + L$ over the admissible interval (for example $v \in [0, 1]$) ensures a unique solution. For the saturating choice

$$f_{\text{sat}}(v) = \frac{\alpha v^2}{1 + \kappa v^2}, \quad \alpha > 0, \kappa > 0, \quad (55)$$

the slope

$$f'_{\text{sat}}(v) = \frac{2\alpha v}{(1 + \kappa v^2)^2} \quad (56)$$

is nonnegative and bounded on $[0, 1]$, with $\max_{v \in [0, 1]} f'_{\text{sat}}(v) \leq \frac{3\sqrt{3}}{8} \frac{\alpha}{\sqrt{\kappa}}$. If

$$\inf_{v \in [0, 1]} (f'_{\text{sat}}(v) + L) > 0, \quad (57)$$

then F is strictly increasing on $[0, 1]$ and has at most one root there. If in addition $F(0)F(1) \leq 0$, a unique $v_i^* \in [0, 1]$ exists. Condition (57) is met whenever

$$L > -\frac{3\sqrt{3}}{8} \frac{\alpha}{\sqrt{\kappa}}, \quad (58)$$

which is the small-signal service-dominance requirement: linear damping $\lambda + \chi + \frac{ab}{a+\mu}$ must exceed the maximal small-signal excitability slope.

Networking interpretation. Equation (51) balances offered load against service and damping. The term I_i^* aggregates graph-local arrivals and policy weights; L collects all linear drains. The sensitivity to slowly varying load follows by implicit differentiation:

$$\frac{\partial v_i^*}{\partial I_i^*} = -\frac{1}{f'_{\text{sat}}(v_i^*) + L}. \quad (59)$$

Hence the DC gain is stable and interpretable. It shrinks as saturation increases ($\kappa \uparrow$) or as service and damping increase ($\lambda, \chi, ab/(a + \mu) \uparrow$), which matches the operational goal of keeping the queue operating point insensitive to modest load drift.

K.2 Jacobian and linear stability (details)

Linearising *NOS* node (2)–(3) at a subthreshold equilibrium (v^*, u^*) gives the single-node Jacobian

$$J_i = \begin{bmatrix} f'(v^*) + \beta - \lambda - \chi & -1 \\ ab & -(a + \mu) \end{bmatrix}, \quad (60)$$

with trace and determinant

$$T_i = \text{tr}(J_i) = f'(v^*) + \beta - \lambda - \chi - (a + \mu), \quad (61)$$

$$\Delta_i = \det(J_i) = ab - (f'(v^*) + \beta - \lambda - \chi)(a + \mu). \quad (62)$$

The Routh–Hurwitz conditions for a two-dimensional system yield local asymptotic stability if and only if

$$T_i < 0 \quad \text{and} \quad \Delta_i > 0. \quad (63)$$

Networking reading. The trace condition (63) asks that net drain $(a + \mu) + (\lambda + \chi - \beta)$ exceeds the small-signal growth from $f'(v^*)$. The determinant condition requires that the product of recovery gain ab and time-scale $(a + \mu)$ dominates the same growth term. Together they state that service plus damping and the recovery loop must remove perturbations faster than excitability amplifies them. When either inequality tightens, small oscillations and slow return-to-baseline emerge, which operators observe as ringing in queue telemetry.

Specialisations. *Quadratic small-signal.* For small $|v^*|$, use $f'(v^*) \approx 2\alpha v^*$ and test (63) with that slope.

Bounded excitability. For $f_{\text{sat}}(v) = \frac{\alpha v^2}{1 + \kappa v^2}$,

$$f'(v^*) = \frac{2\alpha v^*}{(1 + \kappa(v^*)^2)^2}, \quad (64)$$

$$T_i = \frac{2\alpha v^*}{(1 + \kappa(v^*)^2)^2} + \beta - \lambda - \chi - (a + \mu), \quad (65)$$

$$\Delta_i = ab - \left(\frac{2\alpha v^*}{(1 + \kappa(v^*)^2)^2} + \beta - \lambda - \chi \right) (a + \mu). \quad (66)$$

As κ grows, the effective slope (64) decreases, enlarging the stability region defined by (63). A full statement and supporting derivations for the stability claims are given in below.

Lemma 1 (Monotone stabilisation by saturation). *Let $f_{\text{sat}}(v) = \frac{\alpha v^2}{1 + \kappa v^2}$ with $\alpha > 0$, $\kappa > 0$, and let $v^* \geq 0$ be a subthreshold equilibrium. Then*

$$\frac{\partial}{\partial \kappa} f'(v^*) = -\frac{4\alpha(v^*)^3}{(1 + \kappa(v^*)^2)^3} \leq 0, \quad (67)$$

with equality only at $v^ = 0$. Consequently,*

$$\begin{aligned} \frac{\partial T_i}{\partial \kappa} &= \frac{\partial f'(v^*)}{\partial \kappa} < 0 \quad (v^* > 0), \\ \frac{\partial \Delta_i}{\partial \kappa} &= -(a + \mu) \frac{\partial f'(v^*)}{\partial \kappa} > 0 \quad (v^* > 0), \end{aligned} \quad (68)$$

so increasing κ strictly decreases the trace and strictly increases the determinant, enlarging the region $\{T_i < 0, \Delta_i > 0\}$.

Proof sketch. Differentiate $f'(v) = \frac{2\alpha v}{(1 + \kappa v^2)^2}$ with respect to κ :

$$\frac{\partial}{\partial \kappa} f'(v) = -\frac{4\alpha v^3}{(1 + \kappa v^2)^3}, \quad (69)$$

which is nonpositive for $v \geq 0$ and strictly negative for $v > 0$. Substituting into (65)–(66) gives (68). \square

Corollary 1.1 (Network threshold increases with saturation). *Under homogeneous coupling $G = gW$ with Perron eigenvalue $\rho(W)$, define*

$$\bar{d} := f'(v^*) + \beta - \lambda - \chi, \quad k^* = \min\left\{(a + \mu) - \bar{d}, \frac{ab}{a + \mu} - \bar{d}\right\}, \quad g_* \approx \frac{k^*}{\rho(W)}. \quad (70)$$

Since $\frac{\partial \bar{d}}{\partial \kappa} = \frac{\partial f'(v^*)}{\partial \kappa} < 0$ for $v^* > 0$, one has $\frac{\partial k^*}{\partial \kappa} > 0$ and therefore $\frac{\partial g_*}{\partial \kappa} > 0$ on the active branch of k^* . Increasing κ raises the coupling needed to destabilise the network, which matches the bounded-excitability design goal.

In networking terms, making the excitability saturate earlier reduces small-signal gain and raises damping, which protects the node against oscillations when operated near capacity.

Operational guidance. When tuning for a given site, estimate v^* from the modal subthreshold queue level and compute the small-signal slope $f'(v^*)$ using the fitted (α, κ) . If (63) is tight, increasing κ (earlier saturation) or increasing λ and χ adds headroom. If tightening occurs only in Δ_i , adjust the recovery loop (a, b, μ) to increase ab or the composite time-scale $(a + \mu)$; both choices shorten the memory of recent stress and prevent ringing after bursts. Decay times and DC sensitivity that guide window length and reset tuning are summarised in below Eqs. (71) and (72).

Eigenvalues and decay times. Let $\lambda_{1,2}$ be the eigenvalues of the local Jacobian J_i defined in K.2. When the Routh–Hurwitz conditions in (63) hold and $T_i^2 > 4\Delta_i$, the node is an overdamped node with two real negative modes. When $T_i^2 < 4\Delta_i$, it is underdamped with complex conjugate modes whose common decay rate is $-\frac{1}{2}T_i$. The dominant linear return time is

$$\tau_{\text{lin}} \approx \frac{1}{\min\{-\Re\lambda_1, -\Re\lambda_2\}}, \quad (71)$$

which provides an engineering handle for truncated BPTT windows and for selecting the reset constant ρ so numerical timescales match device drain and scheduler epochs. In practice, τ_{lin} estimated from small perturbations of I_i around an operating point aligns well with the observed relaxation of the queue proxy v_i .

Input–output small-signal gain. Let \hat{I} be a small constant perturbation of I_i and \hat{v} the induced steady-state change in v_i . Using the equilibrium implicit-function relation from (59), the DC gain is

$$\frac{\hat{v}}{\hat{I}} = -\frac{1}{f'_{\text{sat}}(v^*) + L}. \quad (72)$$

Larger service λ and stronger damping χ decrease this gain, making the operating point less sensitive to slow offered-load drift. This matches queueing intuition and yields a direct calibration target: estimate \hat{v}/\hat{I} from step tests or natural experiments in telemetry, then verify that the inferred L is consistent with the Jacobian conditions in (63).

K.3 Network coupling and global stability (details)

In isolation a *NOS* unit is a load–service balance set by its local parameters. In a network the steady input is shaped by neighbours and policy weights, so existence and robustness of equilibria depend on both the operating point and the coupling matrix. Let $W = [w_{ij}]$ be the graph coupling and let S_j^* denote the effective steady presynaptic drive at node j (after any per–link delays and gates). The steady input at node i is

$$I_i^* = \sum_j w_{ij} S_j^*, \quad \max_i I_i^* \leq \|W\|_\infty \|S^*\|_\infty, \quad \|I_i^*\|_2 \leq \|W\|_2 \|S^*\|_2 \quad (73)$$

with $\|W\|_2 = \sqrt{\rho(W^\top W)}$, and the spectral radius obeys $\rho(W) \leq \|W\|_\infty$, so $\|W\|_\infty$ gives a conservative topology-aware cap on steady drive. From the scalar equilibrium reduction (cf. (49)–(54)), define

$$L := \beta - \lambda - \chi - \frac{ab}{a + \mu}, \quad C := \gamma + \chi v_{\text{rest}} + I_i^*, \quad (74)$$

and write the per-node equilibrium condition as

$$f_{\text{sat}}(v_i^*) + L v_i^* + C = 0. \quad (75)$$

Existence bounds. Two complementary sufficient conditions are useful in operations. *Saturated cap (conservative).* Since $f_{\text{sat}}(v) \leq \alpha/\kappa$ for all v ,

$$C \leq \frac{\alpha}{\kappa} \implies \text{a nonnegative equilibrium exists when } L \leq 0. \quad (76)$$

This bound uses only the saturation ceiling and is independent of the local operating point.

Quadratic small-signal. Approximating $f_{\text{sat}}(v) \approx \alpha v^2$ near light load $v = 0$ gives

$$\alpha (v_i^*)^2 + L v_i^* + C = 0, \quad D_i = L^2 - 4\alpha C, \quad (77)$$

so an equilibrium exists if

$$C \leq \frac{L^2}{4\alpha}. \quad (78)$$

We refer to (78) as the *quadratic small-signal* bound. Combining (78) with the norm bound in (73) yields

$$\gamma + \chi v_{\text{rest}} + \|W\|_\infty \|S^*\|_\infty \leq \frac{L^2}{4\alpha}, \quad (79)$$

with a spectral alternative obtained by replacing $\|W\|_\infty \|S^*\|_\infty$ with $\|W\|_2 \|S^*\|_2$. Inequality (79) makes the graph explicit: heavier row sums (dense fan–in or large policy weights) shrink headroom for the same steady S^* .

Operational margin. A convenient scalar indicator is

$$\Delta_{\text{op}} := \frac{L^2}{4\alpha} - (\gamma + \max_i I_i^*), \quad (80)$$

which is positive when the quadratic small-signal existence test passes with slack. In practice, keeping $\Delta_{\text{op}} > 0$ under nominal load provides headroom for burstiness and guides weight normalisation: scale W so that the largest row sum keeps $\max_i I_i^*$ below the right-hand side of (79). When delays τ_{ij} are present, (79) remains a conservative existence test; sharper delay-aware guarantees require the block Jacobian in the next subsection.

Operational margin under load and damping. The operational margin (80) can be plotted as a function of the subthreshold damping χ and the maximum steady input $I_{\max} = \max_i I_i^*$, as in Fig. 2. The red contour $\Delta_{\text{op}} = 0$ separates admissible operating points from those that violate the quadratic small-signal bound. From a networking viewpoint, χ measures the strength of subthreshold queue relaxation, while I_{\max} is the heaviest sustained offered load after graph coupling. Two effects are visible: (i) the margin decreases monotonically with I_{\max} , so higher offered load erodes headroom; (ii) larger χ shifts the boundary outward, permitting higher sustained load before crossing $\Delta_{\text{op}} = 0$. Stronger damping therefore improves resilience but does not remove the inherent load–margin trade-off. $\|W\|_{\infty}$ aggregates worst–case inbound influence at a node, so it reflects heavy in–degree or imbalanced policies; $\|W\|_2$ captures coherent multi–hop reinforcement. Both provide simple levers: reweight heavy rows, sparsify fan–in, or gate selected edges until Δ_{op} is positive with a chosen margin.

Illustrative computation. Using the legacy “starter” values (kept here for continuity) $\alpha = 0.02$, $\beta = 0.5$, $\gamma = 0.05$, $\lambda = 0.2$, $a = 0.05$, $b = 0.5$, $\mu = 0.01$, $\chi = 0.05$, and $I_{\max} = 0.10$,

$$\frac{ab}{a + \mu} = \frac{0.025}{0.06} \approx 0.4167, \quad L = 0.5 - 0.2 - 0.05 - 0.4167 \approx -0.1667,$$

$$\frac{L^2}{4\alpha} \approx \frac{0.02778}{0.08} = 0.34722, \quad \Delta_{\text{op}} \approx 0.34722 - (0.05 + 0.10) = 0.19722 > 0.$$

At $I_{\max} = 0.30$ the margin is $\Delta_{\text{op}} \approx 0$, and raising χ from 0.05 to 0.30 changes L from -0.1667 to -0.4167 , yielding $\Delta_{\text{op}} \approx 1.82$ —a substantial safety increase. *Note:* these numbers are purely illustrative for the quadratic surrogate; in the main experiments we use the admissible ranges in Table 4. The linear dependence on I_{\max} and the monotone effect of χ hold in either case.

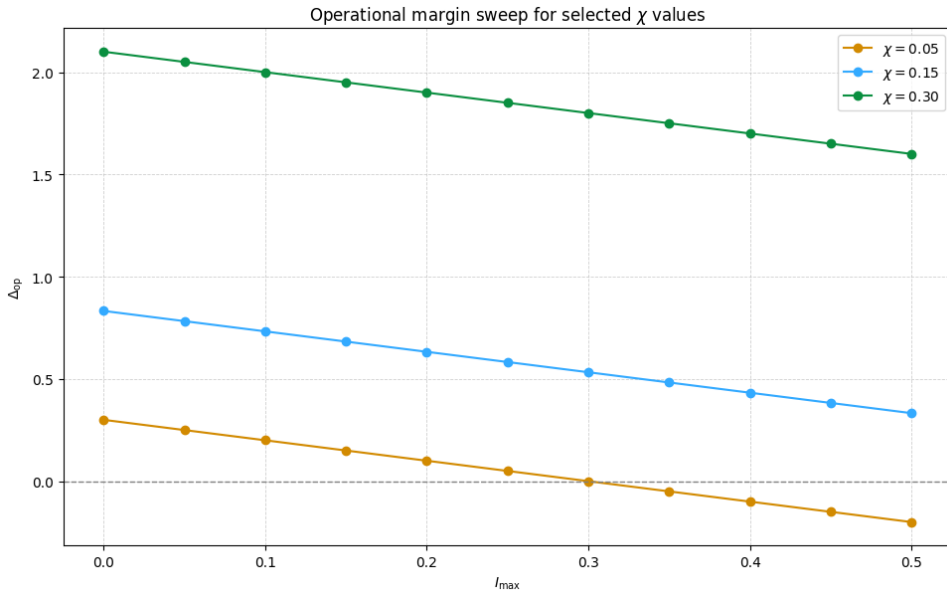


Figure 12: One-dimensional sweeps of the operational margin Δ_{op} against I_{\max} for selected χ . Each trace is affine with slope -1 , illustrating the linear decay of margin with load. Intercepts grow with χ , consistent with the global stability boundary in Fig. 2.

Supporting sweeps. Figure 12 shows Δ_{op} against I_{max} for several χ . The slope is -1 by construction; increasing χ shifts the intercept upward (analogous to higher service slack). For the legacy starter set above the margin crosses zero near $I_{\text{max}} \approx 0.30$, consistent with $\Delta_{\text{op}} = \frac{L^2}{4\alpha} - (\gamma + I_{\text{max}})$, L fixed. Increasing χ increases $|L|$ and hence the scalar margin.

K.4 Block Jacobian, network spectrum, and stability threshold (details)

We assess global small-signal stability by linearising the coupled *NOS* network about a subthreshold equilibrium (v^*, u^*) . Let δv and δu be perturbations of state, and let small variations of presynaptic drive satisfy $\delta I \approx G \delta v$, where G is the input-output sensitivity induced by topology (for homogeneous scaling, $G = gW$). Linearisation of (2)–(3) then yields the $2N \times 2N$ block Jacobian

$$\mathcal{J} = \begin{bmatrix} D + G & -\mathbf{I}_N \\ aB & -(a + \mu)\mathbf{I}_N \end{bmatrix}, \quad D = \text{diag}(f'(v_i^*) + \beta - \lambda - \chi), \quad B = b\mathbf{I}_N. \quad (81)$$

Instability occurs when any eigenvalue of \mathcal{J} crosses into the open right half-plane.

Perron-mode reduction under homogeneous coupling. For homogeneous coupling $G = gW$ with $g \geq 0$ and let $\rho(W)$ be the spectral radius with Perron eigenpair $(\rho(W), \phi)$. Projecting (81) onto ϕ yields an effective 2×2 Jacobian

$$J_{\text{eff}}(k) = \begin{bmatrix} \bar{d} + k & -1 \\ ab & -(a + \mu) \end{bmatrix}, \quad k := g\rho(W), \quad \bar{d} := \frac{1}{\|\phi\|_2^2} \sum_i \phi_i^2 [f'(v_i^*) + \beta - \lambda - \chi]. \quad (82)$$

In the Perron-mode reduction we define $\bar{d} := \frac{1}{\|\phi\|_2^2} \sum_i \phi_i^2 [f'(v_i^*) + \beta - \lambda - \chi]$, which is exact for heterogeneous equilibria. Throughout the subsequent analysis we write $\bar{d} \approx f'_{\text{sat}}(v^*) + \beta - \lambda - \chi$ for homogeneous or mildly heterogeneous whenever $v_i^* \approx v^*$ across nodes (or the Perron vector is sufficiently delocalised). All threshold formulas (e.g. (83) and (85)) remain valid with either form by substituting the appropriate \bar{d} for the deployment at hand. The Routh–Hurwitz conditions for $J_{\text{eff}}(k)$ give the critical scalar coupling

$$k^* = \min \left\{ (a + \mu) - \bar{d}, \frac{ab}{a + \mu} - \bar{d} \right\}, \quad g_* \approx \frac{k^*}{\rho(W)}. \quad (83)$$

Using $\Lambda := \lambda + \chi + \frac{ab}{a + \mu} - \beta$ (cf. (99)), the threshold condition can be written as

$$g\rho(W)f'_{\text{sat}}(v^*) < \Lambda, \quad (84)$$

which matches the stability proxy introduced in the scaling discussion. While the Perron-mode reduction yields tight thresholds in practice, conservative certificates can be obtained via Gershgorin discs and norm bounds; see *methods* K.5 for the resulting inequalities and their comparison to measured g_* in Table 6.

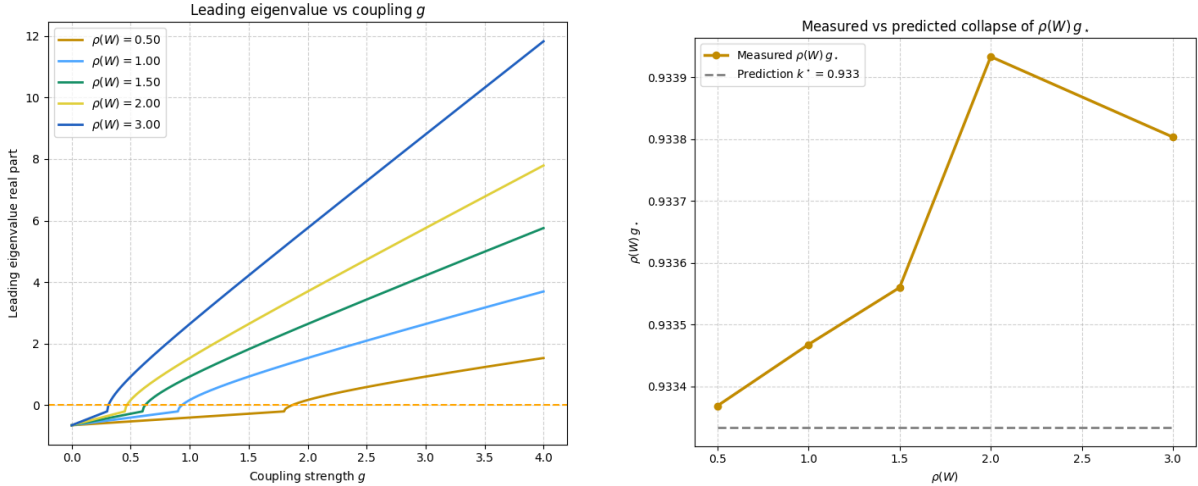


Figure 13: Spectral verification for homogeneous coupling $G = gW$. Left: real part of the leading eigenvalue of the block Jacobian versus g for several $\rho(W)$; the zero crossing defines g_* . Right: collapse of $\rho(W)g_*$ to the scalar threshold k^* predicted by the Perron–mode reduction in (83). The small spread reflects finite size and random matrix variability.

Networking interpretation and control. Figure 13 shows that the first loss of stability is governed by the Perron mode of W . As coupling g increases, the leading eigenvalue crosses the imaginary axis at g_* , marking the onset of coherent queue growth along the dominant influence path. The collapse of $\rho(W)g_*$ onto k^* confirms the separation of concerns in (83): $\rho(W)$ captures how strongly topology reinforces load; k^* depends only on node physics through (\bar{d}, a, b, μ) . Operationally, the levers are direct. Reduce $\rho(W)$ by reweighting heavy fan-in or pruning selected edges. Reduce g through gain scheduling on stressed regions or policy throttles that weaken $I \mapsto v$ sensitivity. Raise the drain margin Λ by increasing service λ , adding subthreshold damping χ , or shortening recovery via a (with b, μ setting the trade). Because $f'_{\text{sat}}(v^*)$ decreases as saturation strengthens (larger κ), bounded excitability expands the stable range in (84).

Finite-size and heterogeneity effects. The rescaled thresholds are not perfectly flat. They sit slightly above k^* across $\rho(W)$, with larger deviations in smaller or more heterogeneous graphs. Two mechanisms explain this percent-level bias. First, nearby non-Perron modes and row-sum variability shift the leading root when the Perron vector localises on hubs, a common feature of heavy-tailed topologies. Second, discrete sweeps of $\Re \lambda_{\max}(g)$ and mild non-normal amplification nudge the numerical crossing. These are finite-size corrections, not a change of scaling, and they diminish with larger N or more homogeneous weights. For conservative guarantees during early deployment, replace $\rho(W)$ by norm bounds or apply Gershgorin discs to \mathcal{J} to obtain stricter, topology-aware thresholds. For deployments requiring analytic guarantees, *methods* K.5 derives Gershgorin and $\|W\|_{\infty}$ -based bounds and reports their conservatism relative to measured g^* (Table 6). A detailed discussion on the bifurcation structure for *NOS*, and its operational interpretation, is given in L.

K.5 Conservative stability via Gershgorin and norm bounds

Let $G = gW$ with $W_{ii} = 0$ and $\rho(W)$ the spectral radius after normalisation (we use $\rho(W) = 1$ in experiments). Linearising (2)–(3) at (v^*, u^*) gives a $2N \times 2N$ block Jacobian \mathcal{J} . For the top block rows 1:N,

$$\bar{d}_i := f'_{\text{sat}}(v_i^*) + \beta - \lambda - \chi,$$

is the diagonal entry, and the off-diagonals are gW_{ij} for $j \neq i$, plus the coupling to u_i with derivative -1 . Thus the Gershgorin centre and radius are

$$c_i = \bar{d}_i, \quad R_i = 1 + |g| \sum_{j \neq i} |W_{ij}|.$$

A sufficient condition for those discs to lie strictly in the left half-plane is

$$\Re(c_i) + R_i < 0 \quad \text{for all } i,$$

which yields

$$|g| < \min_i \frac{-\Re(\bar{d}_i) - 1}{\sum_{j \neq i} |W_{ij}|}.$$

For the bottom block rows $N+1:2N$, the centre is $-(a + \mu)$ and the radius is $|ab|$, so a sufficient condition is

$$-(a + \mu) + |ab| < 0.$$

Using $\sum_{j \neq i} |W_{ij}| \leq \|W\|_\infty$ gives the norm variant

$$|g| < \frac{-\min_i \Re(\bar{d}_i) - 1}{\|W\|_\infty}, \quad \text{and} \quad |ab| < a + \mu.$$

These conditions are sufficient (not necessary) and are conservative relative to observed thresholds.

Table 6: Instability thresholds versus network spectral radius for homogeneous coupling $G = gW$. The measured g_\star is the first zero crossing of the leading eigenvalue real part. The product $\rho(W) g_\star$ agrees with the Perron-mode prediction k^\star . Gershgorin bounds are conservative; negative values mean the bound cannot certify stability for any $g \geq 0$. The heuristic $g_{\text{heur}} = k^\star / \|W\|_\infty$ matches the Perron scaling but lacks a guarantee. The last column checks $|ab| < (a + \mu)$.

$\rho(W)$	g_\star (meas.)	$\rho(W)g_\star$	g_{bound} (Gersh.)	g_{heur}	k^\star (scalar)	$(\rho g_\star)/k^\star$	$ ab < (a + \mu)$
0.5	1.881799	0.940900	-0.526097	0.554642	0.940878	1.000023	True
1.0	0.940924	0.940924	-0.263049	0.277321	0.940878	1.000049	True
1.5	0.627452	0.941177	-0.175366	0.184881	0.940878	1.000319	True
2.0	0.470484	0.940969	-0.131524	0.138660	0.940878	1.000097	True
3.0	0.314042	0.942125	-0.087683	0.092440	0.940878	1.001326	True

Table 6 complements the figures: the measured thresholds obey the Perron-mode scaling ($\rho(W)g_\star \approx k^\star$), while Gershgorin discs provide only conservative certificates. From a networking standpoint, the stability boundary is captured by interpretable quantities: the effective small-signal slope (through \bar{d}_i), service and recovery (λ, a, μ, b) setting k^\star , and the graph's spectral radius encoding topology. This bridges low-level queue dynamics with high-level network design, showing how structural and service parameters jointly control the emergence of congestion instabilities.

L Bifurcation Structure, Operational Interpretation, and Finite-Size Behaviour

Loss of stability as the mean input I increases (or as effective coupling $k = g\rho(W)$ grows) is produced by two local mechanisms. They can be diagnosed either from the scalar equilibrium map $F(v) = f_{\text{sat}}(v) + Lv + C(I)$ (fold tests) or from the 2×2 Jacobian at the operating point (Routh–Hurwitz tests).

1. **Saddle–node (SN).** The stable and unstable equilibria coalesce and disappear when the discriminant in (54) satisfies $D_i = 0$. Beyond this point there is no steady operating level: v drifts upward until resets and leakage dominate. In network terms, offered load or coherent reinforcement pushes a node beyond its admissible queue set; the model predicts sustained congestion with intermittent resets rather than recovery to a fixed level.
2. **Hopf.** The Jacobian trace crosses zero while the determinant remains positive ($T_i = 0$, $\Delta_i > 0$), creating a small oscillatory mode. In network terms, queues enter a self-excited cycle whose phase can entrain neighbors through W , producing rolling congestion waves that propagate along high-gain paths.

Parameter trends and admissibility. Continuation of equilibria v^* versus I reproduces queueing intuition and clarifies which onset is available. Increasing the service λ or the subthreshold damping χ shifts both SN and Hopf onsets to larger I (more headroom); increasing excitability α shifts them to smaller I (less headroom). The recovery coupling b controls whether a Hopf branch is admissible: the linear feedback ab must exceed the decay $(a + \mu)^2$ for an oscillatory onset to exist; otherwise only an SN occurs. Figure 14 shows $v^*(I)$ under sweeps of λ , α , and b ; marker coordinates are listed in Table 7. Near-coincident markers correspond to the codimension-two neighborhood $ab \approx (a + \mu)^2$, where a small change in recovery or damping switches the dominant failure mode from smooth tipping (SN) to oscillatory bursts (Hopf).

Empirical collapse. Across graphs, the measured threshold obeys

$$\rho(W)g_\star \approx \min\left\{(a + \mu) - \bar{d}, \frac{ab}{a + \mu} - \bar{d}\right\}, \quad (85)$$

with small upward deviations when the Perron vector localises or row-sums vary; cf. Fig. 13.

Networking interpretation. The two onsets have distinct operational signatures. An SN route produces a clean loss of a steady queue level and sustained saturation. Telemetry shows a monotone climb in v with resets, increased delay variance, and persistent ECN/markings without a clear period. A Hopf route produces narrowband oscillations: queues and drop/mark rates cycle with a characteristic period $\sim 2\pi/\sqrt{\Delta_i - (T_i/2)^2}$ at onset, and neighboring nodes oscillate in phase along the Perron mode of W . These patterns matter for mitigation. To extend stable throughput, raise λ or χ , or reduce α through stronger saturation (larger κ). To avoid self-sustained burstiness, keep ab comfortably larger than $(a + \mu)^2$ by shortening recovery time (a), reducing recovery sensitivity (b) when needed, or adding passive decay (μ). Each lever maps to standard controls: scheduler and line-rate settings (λ), AQM/leak policies (χ), congestion ramp shaping (α, κ), and backoff or pacing aggressiveness (a, b, μ).

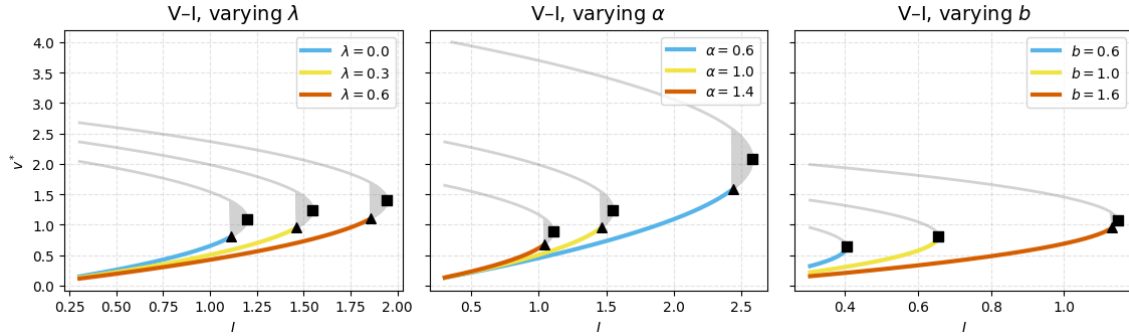


Figure 14: Equilibrium v^* versus input I with saddle-node (■) and Hopf (▲) markers. **(Left)** Increasing service rate λ shifts both onsets to higher I . **(Middle)** Increasing excitability α advances both onsets. **(Right)** Varying recovery coupling b changes the balance between ab and $a + \mu$: when $ab > (a + \mu)^2$ an oscillatory Hopf branch is admissible, otherwise only an SN appears. Stable branches are shown in colour; unstable in faint grey. The exact marker coordinates used here are reported in Table 7.

Table 7: Continuation markers used in Fig. 14. Listed are the input levels I_{SN} and I_{H} and the corresponding equilibria $v_{\text{SN}}^*, v_{\text{H}}^*$. Rows with NaN in the Hopf columns occur where $ab \leq (a + \mu)^2$, so the oscillatory onset is not admissible under the chosen parameters.

Panel	λ	α	b	I_{SN}	v_{SN}^*	I_{H}	v_{H}^*
lambda sweep	0.0	1.0	2.0	1.198	1.095	1.111	0.800
lambda sweep	0.3	1.0	2.0	1.549	1.245	1.462	0.950
lambda sweep	0.6	1.0	2.0	1.945	1.395	1.858	1.100
alpha sweep	0.3	0.6	2.0	2.582	2.074	2.437	1.583
alpha sweep	0.3	1.0	2.0	1.549	1.245	1.462	0.950
alpha sweep	0.3	1.4	2.0	1.106	0.889	1.044	0.679
b sweep	0.3	1.0	0.6	0.404	0.636	NaN	NaN
b sweep	0.3	1.0	1.0	0.656	0.810	NaN	NaN
b sweep	0.3	1.0	1.6	1.146	1.071	1.132	0.950

Finite-size effects and coherence. In finite graphs the transition is slightly rounded but sharpens with size. The measured coupling threshold aligns with the Perron-mode prediction k^* (cf. (83)), with small upward deviations when the Perron vector localises on hubs or when secondary modes lie close in the spectrum. These are percent-level corrections that diminish in larger or more homogeneous topologies. Practically, one can monitor the rescaled margin $\rho(W)g - k^*$: values near zero predict imminent entrainment of queues and the appearance of coherent oscillations along the dominant influence path. Online-Methods O quantifies network coherence via an order parameter $R(t)$, confirming that the onset clusters near k^* and sharpens with N (Fig. 15, Table 8).

Corollary 1.2 (Spectral collapse of the coupling threshold). *For homogeneous coupling $G = gW$, the instability threshold extracted from the block Jacobian satisfies (85), where $\bar{d} = f'_{\text{sat}}(v^*) + \beta - \lambda - \chi$. Percent-level upward deviations arise in finite or heterogeneous graphs when the Perron vector localises or row-sum variability is high, consistent with Fig. 13.*

M Equilibrium and boundedness

At steady state we eliminate u_i using $u_i = \frac{ab}{a+\mu}v_i$ in (3) and obtains a scalar balance:

$$F(v^*) := f_{\text{sat}}(v^*) + L v^* + C = 0, \quad (86)$$

where L and C collect the effective linear and constant drives implied by (2). The next result provides a sufficient, checkable criterion.

Lemma 2 (Existence and uniqueness). *Let $\mathcal{I} \subset \mathbb{R}$ be the admissible queue interval, for example $[0, 1]$. If*

$$\inf_{v \in \mathcal{I}} (f'_{\text{sat}}(v) + L) > 0, \quad (87)$$

then F is strictly increasing on \mathcal{I} and has at most one root. If, in addition, there exist $v_{\pm} \in \mathcal{I}$ with $F(v_-)F(v_+) \leq 0$, then a unique equilibrium $v^ \in \mathcal{I}$ exists. A sufficient global condition is*

$$L > -\frac{3\sqrt{3}}{8} \frac{\alpha}{\sqrt{\kappa}}. \quad (88)$$

Discussion. Condition (87) states that net drain dominates the steepest admissible excitability slope. The bound (88) follows from (34). It is conservative, easy to verify from telemetry, and stable against modest estimation error.

Corollary 2.1 (Algebraic condition and networking view). *For the coefficients in (2)–(3), a sufficient condition for a unique equilibrium in $[0, 1]$ is*

$$\beta - \lambda - \chi - \frac{ab}{a + \mu} > -\frac{3\sqrt{3}}{8} \frac{\alpha}{\sqrt{\kappa}}, \quad (89)$$

or, equivalently,

$$\lambda + \chi + \frac{ab}{a + \mu} > \frac{3\sqrt{3}}{8} \frac{\alpha}{\sqrt{\kappa}} - \beta. \quad (90)$$

Operationally, the left side aggregates service and damping, while the right side is the worst-case excitability minus any linear relief β . At full buffer, service must dominate arrivals; at empty buffer, leakage should not push the queue negative. Hence a single operating point exists within $[0, 1]$.

Engineering rule of thumb. Choose κ so that the knee of f_{sat} lies near the full-buffer scale, for example $1/\sqrt{\kappa} \approx 1$. Fit α from small-signal curvature so that $f_{\text{sat}}(v) \approx \alpha v^2$ around typical loads. Then tune λ and χ to satisfy

$$\lambda + \chi + \frac{ab}{a + \mu} \geq \frac{3\sqrt{3}}{8} \frac{\alpha}{\sqrt{\kappa}} - \beta + \varepsilon, \quad (91)$$

with a small safety margin $\varepsilon > 0$ to absorb burstiness. This keeps the operating point in the unique, stable region and reduces sensitivity to trace noise.

N Non-dimensionalisation and scaling

Operational traces arrive with different bin widths, device rates, and buffer sizes. To make tuning portable across such heterogeneity, we rescale state and time by fixed references V and T , and work with

$$v(t) = V \tilde{v}(\tilde{t}), \quad t = T \tilde{t}, \quad (92)$$

so that \tilde{v} and \tilde{t} are dimensionless queue level and time. This scaling lets parameters fitted on sites with different sampling and buffer sizes be compared on a common basis and leaves the network-level stability proxy $g \rho(W) f'_{\text{sat}}(v^*) < \Lambda$ invariant. Choose V as the full-buffer level used in the queue normalisation (for example, bytes or packets mapped to $v \in [0, 1]$), and choose T as the dominant local timescale: the scheduler epoch, the service drain time $1/\lambda$, or the telemetry bin width when that is the binding constraint. With (92), the left-hand side of (2) satisfies

$$\frac{dv}{dt} = \frac{V}{T} \frac{d\tilde{v}}{d\tilde{t}}, \quad (93)$$

and each term on the right-hand side of (2) is re-expressed as a dimensionless group. The bounded excitability transforms as

$$f_{\text{sat}}(v) = \frac{\alpha v^2}{1 + \kappa v^2} \rightarrow \tilde{f}_{\text{sat}}(\tilde{v}) = \frac{T}{V} f_{\text{sat}}(V\tilde{v}) = \frac{\tilde{\alpha} \tilde{v}^2}{1 + \tilde{\kappa} \tilde{v}^2}, \quad \tilde{\alpha} = \alpha TV, \quad \tilde{\kappa} = \kappa V^2. \quad (94)$$

Linear and constant terms scale as

$$\tilde{\beta} = \beta T, \quad \tilde{\lambda} = \lambda T, \quad \tilde{\chi} = \chi T, \quad \tilde{\gamma} = \frac{\gamma T}{V}, \quad \tilde{v}_{\text{rest}} = \frac{v_{\text{rest}}}{V}. \quad (95)$$

The recovery dynamics (3) become

$$\frac{du}{dt} = a(bv - u) - \mu u \rightarrow \frac{d\tilde{u}}{d\tilde{t}} = \tilde{a}(\tilde{b}\tilde{v} - \tilde{u}) - \tilde{\mu}\tilde{u}, \quad \tilde{a} = aT, \quad \tilde{\mu} = \mu T, \quad \tilde{b} = b, \quad \tilde{u} = \frac{u}{V} \quad (96)$$

and the graph-local input (1) and its delayed form (6) scale as

$$\tilde{I}_i(\tilde{t}) = \frac{T}{V} I_i(t), \quad \tilde{\tau}_{ij} = \frac{\tau_{ij}}{T}, \quad \tilde{w}_{ij} = w_{ij} \quad (\text{dimensionless by construction}). \quad (97)$$

For the shot-noise drive (40), amplitudes and smoothing follow

$$\tilde{\eta}_i(\tilde{t}) = \frac{T}{V} \eta_i(t) = \sum_{n=1}^{N_i(t)} \tilde{A}_{i,n} \tilde{\kappa}_s(\tilde{t} - \tilde{t}_{i,n}), \quad \tilde{A}_{i,n} = \frac{T}{V} A_{i,n}, \quad \tilde{\kappa}_s(\tilde{t}) = e^{-\tilde{t}/\tilde{\tau}_s} H(\tilde{t}), \quad \tilde{\tau}_s = \frac{\tau_s}{T}. \quad (98)$$

With (92)–(98), raw telemetry from sites that sample at 1 ms and sites that sample at 10 ms are mapped to the same dimensionless dynamics. The same holds for devices with different buffers: picking V from the local full-buffer level preserves the meaning of $\tilde{v} \in [0, 1]$. Operators can therefore compare fitted parameters across topologies and hardware: $\tilde{\lambda}$ reflects service relative to the chosen time base; \tilde{a} reflects recovery rate in scheduler units; $\tilde{\alpha}$ and $\tilde{\kappa}$ capture the curvature and knee of the congestion ramp independent of absolute queue size. Delays and gates adopt the same rule: $\tilde{\tau}_{ij}$ is RTT-free propagation and processing in units of T , while w_{ij} stays a policy or bandwidth proportion that is already dimensionless.

Reading guide and forward links. The local slope bound in (34) and the service-damping aggregate in (90) feed directly into the small-signal analysis in K.2 and the network coupling results in §3.3. Let $\rho(W)$ be the spectral radius of the coupling matrix and g any global gain applied to W . Linearisation of (2)–(3) about an operating point v^* yields a block Jacobian whose dominant network term is proportional to $g\rho(W)f'_{\text{sat}}(v^*)$. Compare this against the net drain

$$\Lambda := \lambda + \chi + \frac{ab}{a + \mu} - \beta, \quad (99)$$

which is the left side of (90) minus the right side at the operating point. A convenient stability proxy is

$$g\rho(W)f'_{\text{sat}}(v^*) < \Lambda. \quad (100)$$

Under the rescaling (92), both sides scale by the same factor: Tf'_{sat} and $T\Lambda$ are dimensionless, so (100) is invariant and can be checked in either set of units. The proxy exposes the same levers used in operations. One can reduce $\rho(W)$ by reweighting or sparsifying couplings, reduce g through gain scheduling, or raise Λ by increasing service λ , damping χ , or the recovery rate a (with the trade-off set by b and μ). It is useful to track the *operational margin*

$$\Delta_{\text{net}} := \Lambda - g\rho(W)f'_{\text{sat}}(v^*), \quad (101)$$

which we will use in §3.3 to explain bifurcation onsets, headroom under topology changes, and how weight normalisation can enforce a fixed margin across deployments. Practical rules to meet a target margin are collected in *methods* D.

Operational interpretations and data-driven initialisation of *NOS* parameters from observed network metrics are summarised in Table 3 in *methods* C. The consequences of the chosen scaling for parameter admissibility, together with recommended calibration conventions, follow the same dimensionless groups.

O Finite-size sharpening and synchrony order parameter

Finite networks smooth the bifurcation transitions seen in the scalar reduction. We quantify collective timing with a Kuramoto-type order parameter

$$R(t) = \frac{1}{N} \left| \sum_{j=1}^N e^{i\phi_j(t)} \right|,$$

where spike phases $\phi_j(t)$ are obtained by linear phase interpolation between successive spikes of node j (phase resets to 0 at a spike, advances to 2π at the next). Figure 15 plots the time average $\langle R \rangle$ against the effective coupling $k = g\rho(W)$ for several network sizes N . The curves show the expected S-shaped rise: for small k the system is desynchronised and $\langle R \rangle$ is low; once k passes a critical value the order parameter increases rapidly and then saturates.

The dashed line marks the Perron-mode prediction k^* from the linear analysis of *NOS*. Across N , measured onsets cluster near k^* . Finite-size effects smooth the transition for small N and sharpen it as N grows, while the turning point remains anchored by k^* .

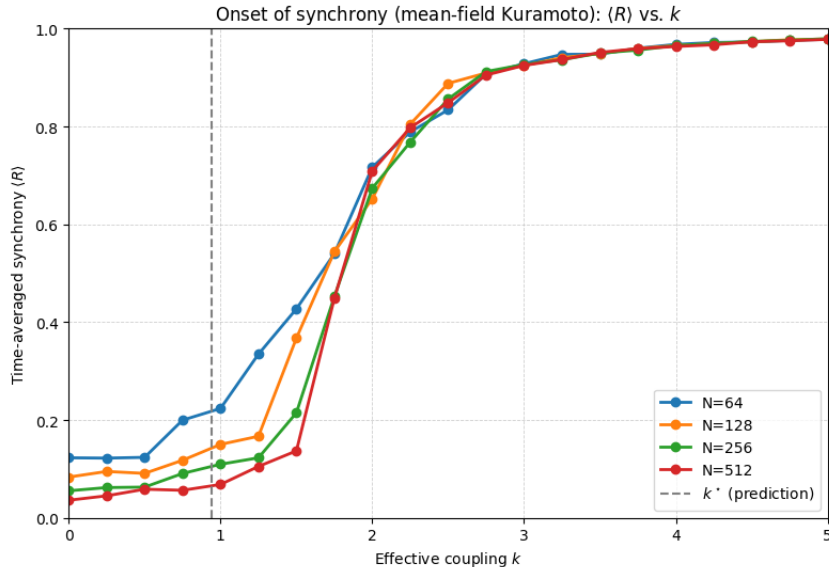


Figure 15: Onset of synchrony in *NOS*. Time-averaged order parameter $\langle R \rangle$ versus effective coupling $k = g \rho(W)$ for several network sizes N . The dashed line marks the Perron-mode prediction k^* . The transition sharpens with N , while the onset remains close to k^* .

Networking interpretation. Synchrony corresponds to queueing cycles that align across nodes: burst build-up and drain events become temporally coordinated. Below k^* these cycles are weakly correlated and buffers clear largely independently. Near and above k^* , coupling is strong enough for delayed spikes to propagate and reinforce, producing network-wide burst trains. Because $k = g \rho(W)$, stability can be preserved either by reducing the local coupling gain g (e.g. weight attenuation or stronger subthreshold leak) or by reducing the spectral radius $\rho(W)$ (e.g. reweighting or sparsifying high-gain pathways). Both actions move the operating point away from the synchrony threshold.

P Zero-shot forecasting baselines (no labels)

Setup (like-for-like, no training). All methods receive the same sliding window of arrival counts (last L bins per node) and must predict the next queue sample q_{t+1} *without supervised training*. We include: (**Phys.-Fluid**) the label-free fluid update $q_{t+1} = \text{clip}(q_t + a_t - \mu \Delta t)$; (**MovingAvg**) a smoothed fluid variant; (**TGNN-smooth**) a single-hop temporal-graph smoother applied to arrivals before the fluid step; (**LIF-leaky**) a leaky-integrator forecaster; and (**NOS (calibr.)**) a single *NOS* unit per node with *arrival-only* calibration (no queue labels): a global input gain and per-node output scales are fitted to match light-load analytic means from M/M/1. In the run summarized here we obtained $\text{gain}_I = 0.60$ and the first three per-node scales $\{11.646, 12.226, 12.277\}$; the corresponding analytic light-load means for those nodes were $\{0.655, 0.738, 0.745\}$ (reported for reference only).

What the figure shows. Figure 16 overlays the *true* queue on node 0 (black) with the five zero-shot forecasts. Phys.-Fluid (blue) tracks the envelope of bursts because it integrates the *same* arrivals that drive the queueing simulator; MovingAvg (orange) lags

Table 8: Representative values of $\langle R \rangle$ at selected couplings k and sizes N (extracted from Fig. 15). The increase of $\langle R \rangle$ with k and the steeper change for larger N reflect finite-size sharpening near k^* .

N	k	$\langle R \rangle$
64	0.0	0.100
64	1.0	0.207
64	2.0	0.822
128	0.0	0.059
128	1.0	0.148
128	2.0	0.769
256	0.0	0.061
256	1.0	0.082
256	2.0	0.755

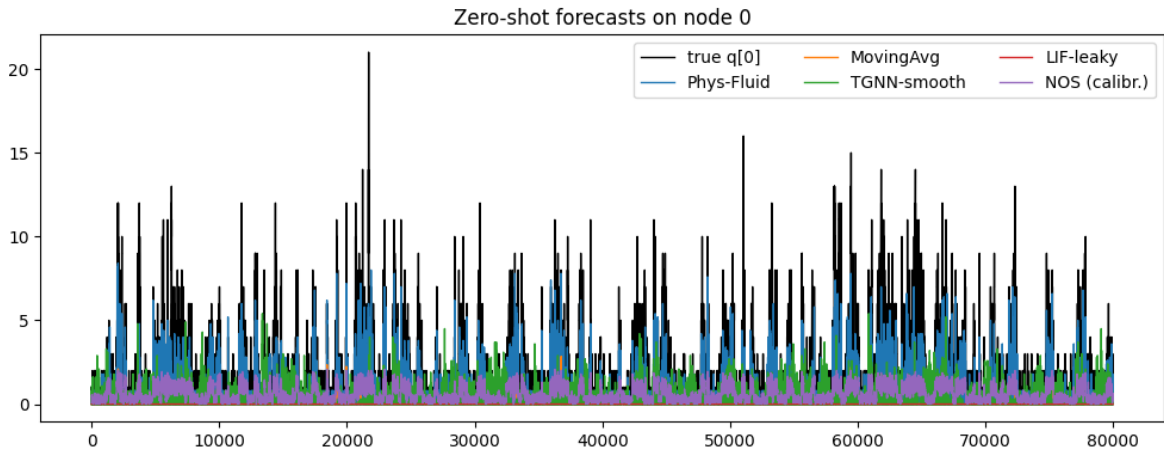


Figure 16: Zero-shot next-step forecasts on a single node (no supervised training). All methods consume the same arrival windows; only *arrival-only* calibration is used. *NOS* produces compact, onset-aligned responses; the fluid forecaster follows backlog accumulation.

and underestimates peaks; TGNN-smooth (green) damps spikes via spatial smoothing; LIF-leaky (red) behaves as a low-pass filter; NOS (purple) fires promptly at burst onsets and then resets, producing compact predictions around excursions.

Numerical summary. Table 9 reports point error (MAE) and event skill (AUROC / AUPRC for top-10% bursts), computed on the same held-out segment. Phys.-Fluid attains the smallest MAE (0.675)—expected, since the simulator itself is fluid-like at the bin scale. NOS has a larger MAE (0.928) because it is *bounded* and self-resets (it does not accumulate backlog), yet it delivers strong event skill (AUROC 0.894, AUPRC 0.536), on par with Phys.-Fluid and substantially above simple smoothers. Operationally, this means *NOS* is well-tuned to *detect and time* congestion onsets without drifting into long false positives between bursts. TGNN-smooth and LIF-leaky reduce noise but lose timing contrast (near-chance event skill).

Table 9: Zero-shot next-step forecasting (no supervised training). All methods use the same arrival windows; *NOS* uses only arrival-based calibration.

Method	MAE	AUROC	AUPRC
Physics Fluid	0.6748	0.834	0.555
Moving Avg	0.8782	0.552	0.194
TGNN-smooth	0.9251	0.507	0.128
LIF-leaky	0.8891	0.500	0.126
NOS (calibr.)	0.9278	0.894	0.536

Networking interpretation. In the absence of labels, a fluid predictor provides a tough MAE baseline because it integrates exactly the arrivals that create the queue, essentially reproducing backlog drift. However, operators often care more about *timely onset detection* than about matching every backlog micro-fluctuation. Here NOS’ bounded, event-driven dynamics produce high AUROC/AUPRC—accurate timing of burst onsets and compact responses—while avoiding prolonged marking during recoveries. This complements the open/closed-loop results: use fluid logic for gross throughput accounting, and deploy *NOS* to deliver low-latency, low-ringing congestion signals aligned with control actions.

Q Evaluation protocol for forecasting baselines

This section details the protocol used for the comparisons in 4.2. For metrics we use networks of size $N=250$; the range plots show node 0 for visual clarity. All baselines are trained label-free on next-step forecasting with a contiguous train/validation/test split. Inputs are standardised per node using statistics fitted on the train split only. Residuals are signed and z -scored with train-only moments; event starts are the first samples whose residual z -scores cross a fixed per-node threshold selected on the validation split but computed using train calibration. Episodes have a minimum duration to suppress single-sample blips; matching uses a fixed window around each ground-truth start. Start-latency is the sample difference between the truth start and the first model start within the window, converted to milliseconds using the sampling period Δt . Forecasting error (MAE, RMSE) is computed on the original scale. The tGNN uses temporal message passing constrained to the given adjacency; capacities and early-stopping are held comparable across baselines.

All learned baselines, namely MLP, RNN, GRU, and tGNN, are trained self-supervised on next-step forecasting, and events are inferred from forecast error rather than labels. Train-only calibration prevents leakage and keeps thresholds comparable across models and topologies. The evaluation can be extended with extreme-value thresholds on residual tails, rolling-origin splits to test drift, precision–recall curves, episode-wise latency in milliseconds, and an out-of-distribution topology block, without changing the core protocol.

R *NOS* simulation pseudocode

For reproducibility we include the simulation routine used in our experiments. We simulate *NOS* in discrete time with a fixed step dt (forward Euler). Per-edge propagation delays are implemented using delay buffers that store scheduled spike arrivals. Each time step consists of four stages: (i) deliver scheduled arrivals from buffers, (ii) compute the total input from delivered arrivals plus exogenous drive, (iii) update (v, u) using bounded excitability with two leak terms, and (iv) apply thresholding with optional jitter and a soft exponential reset. Throughout, $S_{j \rightarrow i}^{\text{del}}(t) \in \{0, 1\}$ denotes the spike arrival delivered to node i on edge $(j \rightarrow i)$ at time step t .

We use both leak terms in the membrane update: $-\lambda v$ represents a direct drain proportional to the current load, while $-\chi(v - v_{\text{rest}})$ pulls the state back toward the resting level. A bounded excitability nonlinearity $f_{\text{sat}}(\cdot)$ and an optional clamp $v \in [v_{\text{rest}}, v_{\text{max}}]$ prevent runaway growth and reflect finite buffer capacity. The exogenous drive $\eta_i(t)$ may be implemented as shot noise (arrival impulses) or as additive noise; the pseudocode treats it abstractly.

```
# NOS simulation with per-edge delay buffers (forward Euler)

# Parameters: dt, T
# States: v[i], u[i]
# Buffers: delay_buffer[i->k] stores scheduled arrivals (0/1) in integer bins

# Initialisation
for each node i:
    v[i] = v_rest + small_noise()
    u[i] = u0

for each directed edge (j -> i):
    L_ij = ceil(tau_ij / dt)
    delay_buffer[j->i] = RingBuffer(length=L_ij)

# Main loop
for t in time_steps: # physical time is t*dt
    # (1) deliver scheduled arrivals and build synaptic input
    for each node i:
        I_syn[i] = 0

    for each directed edge (j -> i):
        S_del = delay_buffer[j->i].pop()
        I_syn[i] += W[i,j] * gate(q_ij, t) * S_del

    # (2) exogenous drive
    for each node i:
        I_ex[i] = eta(i, t)
        I[i] = I_syn[i] + I_ex[i]

    # (3) Euler update from old state (uses both leak terms)
    for each node i:
```

```

v_old = v[i]
u_old = u[i]

v_new = v_old + dt * ( f_sat(v_old) + beta*v_old + gamma - u_old
                      + I[i] - lambda*v_old - chi*(v_old - v_rest) )
u_new = u_old + dt * ( a*(b*v_old - u_old) - mu*u_old )

v[i] = clip(v_new, v_rest, v_max)
u[i] = clip(u_new, u_min, u_max)
for each node i:
    v_th_eff = v_th + sigma * randn()
    if v[i] >= v_th_eff:
        emit_spike(i, t*dt)
        for each outgoing edge (i -> k):
            delay_buffer[i->k].push(1)
        v[i] = c + (v[i] - c) * exp(-r_reset * dt)
        u[i] = u[i] + d

# Record observables as needed (rates, ISI CV, avalanches, synchrony).

```

References

- [1] L. F. Abbott, B. DePasquale, and R. M. Memmesheimer. Building functional networks of spiking model neurons. *Nature Neuroscience*, 19:350–355, 2016.
- [2] Mohammed Ahmed, Abdulkadir N. Mahmood, and Jiankun Hu. A survey of network anomaly detection techniques. *Journal of Network and Computer Applications*, 60:19–31, 2016.
- [3] Nehal Baganal-Krishna, Ralf Lübben, Eirini Liotou, Konstantinos V. Katsaros, and Amr Rizk. A federated learning approach to qos forecasting in cellular vehicular communications: Approaches and empirical evidence. *Computer Networks*, 242:110239, 2024.
- [4] Dennis Bäßler, Tobias Kortus, and Gabriele Gühring. Unsupervised anomaly detection in multivariate time series with online evolving spiking neural networks. *Machine Learning*, 111(4):1377–1408, 2022.
- [5] Tianshi Chen, Zidong Du, Ninghui Sun, Jia Wang, Chengyong Wu, Yunji Chen, and Olivier Temam. A high-throughput neural network accelerator. *IEEE Micro*, 35(3):24–32, 2015.
- [6] S. S. Chowdhury, D. Sharma, A. Kosta, et al. Neuromorphic computing for robotic vision: algorithms to hardware advances. *Communications Engineering*, 4:152, 2025.
- [7] M. Davies et al. Loihi: A neuromorphic manycore processor with on-chip learning. *IEEE Micro*, 38(1):82–99, 2018.
- [8] Steve B. Furber, Francesco Galluppi, Steve Temple, and Luis A. Plana. The spinnaker project. *Proceedings of the IEEE*, 102(5):652–665, 2014.

- [9] Steve B. Furber, Francesco Galluppi, Steve Temple, and Luis A. Plana. The spinaker project. *Proceedings of the IEEE*, 102(5):652–665, 2014.
- [10] E. Gelenbe. G-networks: a unifying model for neural and queueing networks. *Annals of Operations Research*, 48:433–461, 1994.
- [11] Erol Gelenbe. Random neural networks with negative and positive signals and product form solution. *Neural Computation*, 1(4):502–510, 1989.
- [12] Erol Gelenbe. Stability of the random neural network model. *Neural Computation*, 2(2):239–247, 1990.
- [13] Anna Giannakou, Dipankar Dwivedi, and Sean Peisert. A machine learning approach for packet loss prediction in science flows. *Future Generation Computer Systems*, 102:190–197, 2020.
- [14] Lei Guo, Dongzhao Liu, Youxi Wu, and Guizhi Xu. Comparison of spiking neural networks with different topologies based on anti-disturbance ability under external noise. *Neurocomputing*, 529:113–127, 2023.
- [15] M. Häusser. The Hodgkin-Huxley theory of the action potential. *Nature Neuroscience*, 3(Suppl 11):1165, 2000.
- [16] Adeel Iqbal, Ali Nauman, Riaz Hussain, and Muhammad Bilal. Cognitive d2d communication: A comprehensive survey, research challenges, and future directions. *Internet of Things*, 24:100961, 2023.
- [17] E. M. Izhikevich. Simple model of spiking neurons. *IEEE Transactions on Neural Networks*, 14(6):1569–1572, 2003.
- [18] Jieliang Jiang, Jiale Zhu, Muhammad Bilal, Yan Cui, Neeraj Kumar, Ruihan Dou, Feng Su, and Xiaolong Xu. Masked swin transformer unet for industrial anomaly detection. *IEEE Transactions on Industrial Informatics*, 19(2):2200–2209, 2023.
- [19] Jann Krausse, Daniel Scholz, Felix Kreutz, Pascal Gerhards, Klaus Knobloch, and Jürgen Becker. Extreme sparsity in hodgkin-huxley spiking neural networks. In *2023 International Conference on Neuromorphic Computing (ICNC)*, pages 85–94, 2023.
- [20] N. Langlois, P. Miche, and A. Bensch. Analogue circuits of a learning spiking neuron model. In *Proceedings of the IEEE-INNS-ENNS International Joint Conference on Neural Networks. IJCNN 2000. Neural Computing: New Challenges and Perspectives for the New Millennium*, volume 4, pages 485–489 vol.4, 2000.
- [21] Honghui Liang, Zhiguang Chen, Yangle Zeng, Guangnan Feng, and Yutong Lu. *DFMG: Delay-Flush Multi-Group Algorithm for Spiking Neural Network Simulation*, page 479–485. Association for Computing Machinery, New York, NY, USA, 2025.
- [22] Chit-Kwan Lin, Andreas Wild, Gautham N. Chinya, Yongqiang Cao, Mike Davies, Daniel M. Lavery, and Hong Wang. Programming spiking neural networks on intel’s loihi. *Computer*, 51(3):52–61, 2018.

- [23] Guoqiang Liu, Guanming Bao, Muhammad Bilal, Angel Jones, Zhipeng Jing, and Xiaolong Xu. Edge data caching with consumer-centric service prediction in resilient industry 5.0. *IEEE Transactions on Consumer Electronics*, 70(1):1482–1492, 2024.
- [24] Nguyen Cong Luong, Dinh Thai Hoang, Shimin Gong, Dusit Niyato, Ping Wang, Ying-Chang Liang, and Dong In Kim. Applications of deep reinforcement learning in communications and networking: A survey. *IEEE Communications Surveys & Tutorials*, 21(4):3133–3174, 2019.
- [25] Piotr S. Maciąg, Marzena Kryszkiewicz, Robert Bembenik, Jesús L. Lobo, and Javier Del Ser. Unsupervised anomaly detection in stream data with online evolving spiking neural networks. *Neural Networks*, 139:118–139, 2021.
- [26] Ahlem Menaceur, Hamza Drid, and Mohamed Rahouti. Fault tolerance and failure recovery techniques in software-defined networking: A comprehensive approach. *Journal of Network and Systems Management*, 31(83), 2023.
- [27] Emre O. Neftci, Hesham Mostafa, and Friedemann Zenke. Surrogate gradient learning in spiking neural networks: Bringing the power of gradient-based optimization to spiking neural networks. *IEEE Signal Processing Magazine*, 36(6):51–63, 2019.
- [28] Thuy T. T. Nguyen and Grenville Armitage. A survey of techniques for internet traffic classification using machine learning. *IEEE Communications Surveys & Tutorials*, 10(4):56–76, 2008.
- [29] Jonathan Platkiewicz, Eran Stark, and Asohan Amarasingham. Spike-centered jitter can mistake temporal structure. *Neural Computation*, 29(3):783–803, 2017.
- [30] Ali Rasteh, Florian Delpech, Carlos Aguilar-Melchor, Romain Zimmer, Saeed Bagheri Shouraki, and Timothée Masquelier. Encrypted internet traffic classification using a supervised spiking neural network. *Neurocomput.*, 503(C):272–282, September 2022.
- [31] Mariana Segovia-Ferreira, Jose Rubio-Hernan, Ana Rosa Cavalli, and Joaquin Garcia-Alfaro. A survey on cyber-resilience approaches for cyber-physical systems. *ACM Computing Surveys*, 56(8):1–37, 2024.
- [32] Laith A. Shamieh, Wei-Chun Wang, Shida Zhang, Rakshith Saligram, Amol D. Gaidhane, Yu Cao, Arijit Raychowdhury, Suman Datta, and Saibal Mukhopadhyay. Cryogenic operation of computing-in-memory based spiking neural network. In *Proceedings of the 29th ACM/IEEE International Symposium on Low Power Electronics and Design*, ISLPED ’24, page 1–6, New York, NY, USA, 2024. Association for Computing Machinery.
- [33] Muhammad Basit Umair, Zeshan Iqbal, Muhammad Bilal, Jamel Nebhen, Tarik Adnan Almohamad, and Raja Majid Mehmood. An efficient internet traffic classification system using deep learning for iot. *Computers, Materials & Continua*, 71(1):407–422, 2022.
- [34] Xiaolong Xu, Chenyi Yang, Muhammad Bilal, Weimin Li, and Huihui Wang. Computation offloading for energy and delay trade-offs with traffic flow prediction in edge computing-enabled iot. *IEEE Transactions on Intelligent Transportation Systems*, 24(12):15613–15623, 2023.

- [35] Zhenyu Xu, Wenxin Li, Aurojit Panda, and Minlan Yu. Teal: Learning-accelerated optimization of WAN traffic engineering. In *Proceedings of the ACM SIGCOMM 2023 Conference*. ACM, 2023.
- [36] Xu Yang, Yunlin Lei, Mengxing Wang, Jian Cai, Miao Wang, Ziyi Huan, and Xialv Lin. Evaluation of the effect of the dynamic behavior and topology co-learning of neurons and synapses on the small-sample learning ability of spiking neural network. *Brain Sciences*, 12(2), 2022.
- [37] Ming Yao, Oliver Richter, Guangyu Zhao, Ning Qiao, Yannan Xing, Dingheng Wang, Tianxiang Hu, Wei Fang, Tugba Demirci, Michele De Marchi, Lei Deng, Tianyi Yan, Carsten Nielsen, Sadique Sheik, Chenxi Wu, Yonghong Tian, Bo Xu, and Guoqi Li. Spike-based dynamic computing with asynchronous sensing-computing neuromorphic chip. *Nature Communications*, 15:4464, 2024.
- [38] Friedemann Zenke and Wulfram Gerstner. Limits to high-speed simulations of spiking neural networks using general-purpose computers. *Frontiers in Neuroinformatics*, 8:76, 2014.
- [39] Jilun Zhang and Ying Liu. Brain-like path planning algorithm based on spiking neural network. In *Proceedings of the 2025 6th International Conference on Computer Information and Big Data Applications*, CIBDA '25, page 1379–1386, New York, NY, USA, 2025. Association for Computing Machinery.
- [40] Jingjing Zhao, Xuyang Jing, Zheng Yan, and Witold Pedrycz. Network traffic classification for data fusion: A survey. *Information Fusion*, 72:22–47, 2021.
- [41] Yuan Zhi, Jie Tian, Xiaofang Deng, Jingping Qiao, and Dianjie Lu. Deep reinforcement learning-based resource allocation for d2d communications in heterogeneous cellular networks. *Digital Communications and Networks*, 8(5):834–842, 2022.

Algorithm 1 Discrete-time simulation of *NOS* dynamics with per-edge delays and soft resets

- 1: **Initialise:** for each node i , set $v_i \leftarrow v_{\text{rest}} + \epsilon$, $u_i \leftarrow u_0$
- 2: **Initialise:** for each directed edge ($j \rightarrow i$), create a delay buffer of length $\lceil \tau_{ij}/dt \rceil$
- 3: **for** each time step t **do**
- 4: **(1) Deliver delayed spikes:** set $I_i^{\text{syn}} \leftarrow 0$ for all i
- 5: **for** each directed edge ($j \rightarrow i$) **do**
- 6: Pop delivered arrival $S_{j \rightarrow i}^{\text{del}}(t)$ from the buffer for ($j \rightarrow i$)
- 7: Accumulate synaptic input: $I_i^{\text{syn}} \leftarrow I_i^{\text{syn}} + w_{ij} g(q_{ij}, t) S_{j \rightarrow i}^{\text{del}}(t)$
- 8: **end for**
- 9: **(2) Total input:** for each node i , set $I_i(t) \leftarrow I_i^{\text{syn}} + \eta_i(t)$
- 10: **(3) State update (forward Euler):** for each node i

$$v_i^{\text{old}} \leftarrow v_i, \quad u_i^{\text{old}} \leftarrow u_i$$

$$v_i \leftarrow v_i^{\text{old}} + dt \cdot \left(f_{\text{sat}}(v_i^{\text{old}}) + \beta v_i^{\text{old}} + \gamma - u_i^{\text{old}} + I_i(t) - \lambda v_i^{\text{old}} - \chi(v_i^{\text{old}} - v_{\text{rest}}) \right)$$

$$u_i \leftarrow u_i^{\text{old}} + dt \cdot \left(a(bv_i^{\text{old}} - u_i^{\text{old}}) - \mu u_i^{\text{old}} \right)$$

- 11: (Optional) clamp: $v_i \leftarrow \text{clip}(v_i, v_{\text{rest}}, v_{\text{max}})$, $u_i \leftarrow \text{clip}(u_i, u_{\text{min}}, u_{\text{max}})$
- 12: **(4) Threshold and reset:** for each node i

$$v_{\text{th},i}(t) \leftarrow v_{\text{th}} + \sigma \xi_i(t) \quad (\xi_i(t) \sim \mathcal{N}(0, 1), \sigma = 0 \text{ for deterministic runs})$$

- 13: **if** $v_i \geq v_{\text{th},i}(t)$ **then**
- 14: Emit spike at time t and record it as $S_i(t) = 1$
- 15: **for** each outgoing edge ($i \rightarrow k$) **do**
- 16: Push an arrival into the buffer for ($i \rightarrow k$) scheduled at $t + \tau_{ik}$
- 17: **end for**
- 18: Soft exponential reset:

$$v_i \leftarrow c + (v_i - c) e^{-r_{\text{reset}} dt}, \quad u_i \leftarrow u_i + d$$

- 19: **end if**
 - 20: **end for**
-